Computational Condensed Matter 41 (2024) e00977

Contents lists available at ScienceDirect

Computational Condensed Matter

journal homepage: www.elsevier.com/locate/cocom

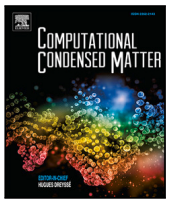

Full length article

Optical properties of rutile TiO_2 with Zr, Mo, Zn, Cd impurities

Kaoru Ohno [a,b,*], Ryoji Sahara [b], Takeshi Nanri [c], Yoshiyuki Kawazoe [d,e,f]

[a] Department of Physics, Graduate School of Engineering, Yokohama National University, 79-5 Tokiwadai, Hodogaya-ku, Yokohama 240-8501, Japan
[b] Research Center for Structural Materials, National Institute for Materials Science (NIMS), 1-2-1 Sengen, Tsukuba, Ibaraki, 305-0047, Japan
[c] Research Institute for Information Technology, Kyushu University, 744 Motooka, Nishi-ku, Fukuoka 819-0395, Japan
[d] New Industry Creation Hatchery Center, Tohoku University, 6-6-4 Aramaki Aza Aoba, Aoba-ku, Sendai, Miyagi, 980-8579, Japan
[e] School of Physics, Institute of Science, Suranaree University of Technology, 111 University Avenue, Nakhon Ratchasima, 30000, Thailand
[f] Physics and Nanotechnology, SRM Institute of Science and Technology, Kattankurathur, Tamil Nadu, 603203, India

ARTICLE INFO

Keywords:
Titania
First principles
Photoabsorption spectra
Quasiparticle
Many-body perturbation theory
k-point sampling

ABSTRACT

To explore quasiparticle (QP) energy gaps and photoabsorption spectra of rutile TiO_2 with nonmagnetic transition metal (Zr, Mo, Zn, Cd) impurities, we conducted a Γ-point only GW + Bethe–Salpeter equation (BSE) calculation on a 72 (or 71) atom supercell. Our findings reveal that Zn and Cd impurities must coexist, at least partly, with oxygen vacancies to maintain charge neutrality. Among the systems considered, Mo, Zn, or Cd doped rutile TiO_2 may exhibit optical absorption and catalytic activity under visible light. The resulting QP energy gaps ($\Delta\varepsilon^{QP}$) and photoabsorption energies (PAEs) are fairly in good agreement with both experimental and theoretical data currently available. The necessary conditions for the applicability of the Γ-point only approach in the GW + BSE framework were found to be: (1) The Γ-point only GW calculation should reproduce a reasonable band gap. (2) The "superficial" exciton binding energy (the diagonal element of $W_{vc;vc} - 2X_{vc;vc}$ between v = VBM and c = CBM, where W and X are the direct and exchange terms of the BSE matrix elements, respectively) must be positive or marginally negative. (3) The "real" exciton binding energy ($\Delta\varepsilon^{QP}$– the lowest PAE) should be positive, even if it is exceptionally small.

1. Introduction

Rutile and anatase are two important polymorphs of TiO_2. Anatase irreversibly reverts to rutile at high temperatures, while rutile is structurally more stable than anatase at elevated temperatures, exhibiting greater strength and stability. In 1972, Fujishima and Honda [1] demonstrated that n-type rutile TiO_2 can facilitate water splitting under illumination, claiming that the material does not suffer degradation. This report sparked significant interest in the semiconductor-electrolyte community [2]. The photocatalytic activity of TiO_2 [3,4] is applicable to water [5] and environmental [6] purification, while dye-synthesized TiO_2 exhibits photovoltaic behavior relevant to solar cells [7]. Moreover, TiO_2 shows antibacterial activity [8], biocompatibility [9], and so on. Rutile is also used in optical materials, ultraviolet (UV)-cut cosmetics, pigments, and colorant, and rutile quartz is used in jewelry. In these applications, the optical properties of the transition metal doped rutile TiO_2 are a central focus, as pure rutile TiO_2 has a wide band gap of 3.3 eV and requires UV radiation to excite electrons from the valence band maximum (VBM) to the conduction band minimum (CBM).

So far, numerous experimental and theoretical investigations have focused on rutile TiO_2 with transition metal impurities. Magnetic transition metal impurities such as Cr, Mn, Fe, Co, Ni, and Ru exhibit interesting behaviors, including properties of dilute magnetic semiconductors [10–13] and enhanced conductivity [14,15], in addition to their optical characteristics [16–18]. In contrast, the optical properties have been the main subject of nonmagnetic transition metal impurities, such as Zr, Mo, Zn, and Cd. A range of studies, encompassing experimental and theoretical (density functional theory (DFT)) approaches, have been carried out for Zr [19–22] and Mo [23–26]. Additionally, several experimental studies focused on Zn [27,28] and Cd [28–30]. DFT calculations have been performed for Mo and Cd by Song et al. [31], for Zn by Saini et al. [32], and for Cd by Sato et al. [33] and Errico et al. [34]. However, all these calculations were based on DFT, which is not suitable for studying excited states.

The Green's function technique in many-body perturbation theory [35,36] provides a robust first-principles approach for determining the quasiparticle (QP) energies of materials, which can be precisely measured experimentally using photoelectron spectroscopy. In Hedin's

* Corresponding author at: Department of Physics, Graduate School of Engineering, Yokohama National University, 79-5 Tokiwadai, Hodogaya-ku, Yokohama 240-8501, Japan.
E-mail address: ohno@ynu.ac.jp (K. Ohno).

https://doi.org/10.1016/j.cocom.2024.e00977
Received 27 August 2024; Received in revised form 28 October 2024; Accepted 28 October 2024
Available online 6 November 2024

set of equations [35], the exchange–correlation component of the self-energy is represented as $\Sigma^{xc} = iGW\Gamma$, where G is the one-particle Green's function and Γ is the vertex function. The dynamically screened Coulomb interaction is expressed as $W = \varepsilon^{-1}v$, where v is the bare Coulomb interaction and $\varepsilon = 1 - vP$ is the dielectric function, with $P = -iGG\Gamma$ serving as the polarization function. Here, it is important to note that the normalization problem of the QP wave functions [37,38] has recently been solved by Nakashima et al. [39]. Furthermore, the theory is not limited solely to the ground state; it is also applicable to excited eigenstates as the initial reference state [40,41]. The simplest approximation is to assume $\Gamma = 1$, which is referred to as the GW approximation [35,42]. The well-known one-shot GW (G_0W_0) approach [43–48], which uses the Kohn–Sham (KS) wave functions and eigenvalues [49] from DFT [50], reproduces a reasonable energy gap. Accurate analysis of excitonic effects and photoabsorption spectra (PAS) necessitates solving the Bethe–Salpeter equation (BSE) [36,51] following the G_0W_0 calculation [52–57]. This comprehensive procedure is recognized as the GW + BSE approach.

When addressing the BSE for periodic crystals, $\boldsymbol{k}$-point sampling is generally employed [54–57]. However, in systems with defects or impurities, the supercell size inevitably becomes substantial, making $\boldsymbol{k}$-point sampling cumbersome and time consuming. For such large supercell systems, it is reasonable to justify the use of the GW + BSE approach without $\boldsymbol{k}$-point sampling. Thus, a Γ-point only GW + BSE calculation [52,53,57–60] would be applicable to extensive supercell systems.

In this paper, we apply the Γ-point only GW + BSE approach to investigate QP energy gaps and PAS of rutile TiO_2 with nonmagnetic transition metal impurities. The main objective is to assess the feasibility of a Γ-point only GW + BSE calculation for crystalline rutile TiO_2, both with and without impurity atoms, using a 72 (or 71) atom supercell. We also identify a typo in the key expression of the electron–hole interaction $W_{vc;v'c'}$ in the BSE in the pioneering papers [51,57]. So, we present a detailed derivation of the correct equation in Appendix. The impurities under consideration include Zr, Mo, Zn, and Cd, with each impurity atom substituting one of the Ti atoms in the supercell. The impurity concentration is $x = 1/24 = 4.2$ at% in the chemical form $Ti_{1-x}M_xO_2$ (where M = Zr, Mo, Zn, Cd). If the impurity concentration increases further, the PAS may change drastically, although we have not performed such calculations. Throughout the course of our calculations, we observed that an oxygen vacancy (OV) must accompany the Zn and Cd impurity atoms. This is due to the instability of Zn^{2+} and Cd^{2+} when placed in the Ti^{4+} substitutional site of TiO_2 without the presence of an OV.

2. Method

After a careful convergence check (see Section 4) for pure rutile TiO_2, we use a 2 × 2 × 3 tetragonal supercell (derived from the six-atom tetragonal primitive cell) in the present study. This supercell has dimensions $a = b = 9.1453$ Å and $c = 8.7767$ Å, including a total of 72 atoms. For the impurity systems, one of the titanium atom is replaced with a Zr, Mo, Zn, or Cd atom. For simplicity, spin polarization (i.e., local magnetic moment) is not considered. Additionally, for the systems with a Zn or Cd impurity atom, we also examine configurations with an OV near the impurity atom.

We use Vienna *ab initio* simulation package (VASP) [61] to optimize the entire supercell and the atomic positions within it, employing the local density approximation (LDA) [49,62] with a plane wave (PW) cutoff energy of 500 eV. For the calculation of optical properties, we adopt the all-electron mixed basis approach [58–60,63–68] using TOMBO program [69], where the one-particle wave functions are expressed as a linear combination of both PWs and atomic orbitals (AOs). All core and (truncated) valence numerical AOs (confined inside the nonoverlapping atomic spheres) are utilized alongside the PWs to describe the electronic states. The eigenvalue problem is solved self-consistently within the LDA [49,62] using approximately 11,000 PWs corresponding to a cutoff energy of 25.9 Ry.

In the one-shot GW approach [43–48], the QP wave functions are approximated by the Kohn–Sham orbitals, denoted as $\phi_c(\boldsymbol{r})$ for conduction (c) and $\phi_v(\boldsymbol{r})$ for core–valence (v) levels. We can separate the GW self-energy $\Sigma_{xc}(\omega)$ (excluding the Hartree term) into the Fock exchange term Σ_x and the correlation term $\Sigma_c(\omega)$, such that $\Sigma_{xc}(\omega) = \Sigma_x + \Sigma_c(\omega)$. Their diagonal matrix elements are expressed, respectively, as

$$\langle \phi_n \,|\, \Sigma_x \,|\, \phi_n \rangle = -\sum_v^{\mathrm{occ}} \int \phi_n^*(\boldsymbol{r})\phi_v(\boldsymbol{r})\,\frac{1}{|\boldsymbol{r}-\boldsymbol{r}'|}\,\phi_v^*(\boldsymbol{r}')\phi_n(\boldsymbol{r}')\,d\boldsymbol{r}d\boldsymbol{r}' \tag{1}$$

and

$$\langle \phi_n \,|\, \Sigma_c(\omega) \,|\, \phi_n \rangle = \int d\boldsymbol{r}d\boldsymbol{r}'\phi_n^*(\boldsymbol{r})\phi_n(\boldsymbol{r}')\,\frac{i}{2\pi}\int_{-\infty}^{\infty} d\omega' e^{-i\omega' 0^+} \times \left[\sum_c^{\mathrm{emp}} \frac{\phi_c(\boldsymbol{r})\phi_c^*(\boldsymbol{r}')}{\omega-\omega'-\varepsilon_c^{\mathrm{LDA}}+i0^+} + \sum_v^{\mathrm{occ}} \frac{\phi_v(\boldsymbol{r})\phi_v^*(\boldsymbol{r}')}{\omega-\omega'-\varepsilon_v^{\mathrm{LDA}}-i0^+}\right] \times \left[W(\boldsymbol{r},\boldsymbol{r}';\omega') - \frac{1}{|\boldsymbol{r}-\boldsymbol{r}'|}\right], \tag{2}$$

where $\varepsilon_c^{\mathrm{LDA}}$ and $\varepsilon_v^{\mathrm{LDA}}$ are the LDA energy eigenvalues, and $W(\boldsymbol{r},\boldsymbol{r}';\omega)$ is the dynamically screened Coulomb interaction. In calculating the correlation term and the polarization function $P = -iGG$, the core contribution is ignored in the occupied (occ) summation, while a large number of empty states are included in the empty (emp) summation: 531 for Cd@rutile, 534 for Mo@rutile, 535 for Zr@rutile and Cd+OV@rutile, 540 for Zn@rutile, 544 for pure rutile and Zn+OV@rutile, totaling 1000 levels including core and valence levels. Hereafter, we refer to rutile TiO_2 doped with impurity A as "A@rutile." The full ω' integration [67] is performed at the GW level, as it has been demonstrated that this integration is particularly necessary for TiO_2 [70]. Then, the QP energies are evaluated using (μ_{xc}^{LDA} being the LDA exchange–correlation potential) [44]

$$\varepsilon_n^{\mathrm{QP}} = \varepsilon_n^{\mathrm{LDA}} + Z_n \langle \phi_n \,|\, \Sigma_{xc}(\varepsilon_n^{\mathrm{LDA}}) - \mu_{xc}^{\mathrm{LDA}} \,|\, \phi_n \rangle \tag{3}$$

with a renormalization factor

$$Z_n = \left[1 - \left.\frac{\partial\langle \phi_n \,|\, \Sigma_{xc}(\omega) \,|\, \phi_n \rangle}{\partial\omega}\right|_{\omega=\varepsilon_n^{\mathrm{LDA}}}\right]^{-1}. \tag{4}$$

In the BSE [51,57,58] within the Tamm–Dancoff approximation [51,57], the singlet excitation energies $\Omega_r^{(\mathrm{s})}$ are obtained by solving the matrix eigenvalue equation

$$\sum_{v',c'} (D_{vc;v'c'} + 2X_{vc;v'c'})\, A_r^{(\mathrm{s})}(v',c') = \Omega_r^{(\mathrm{s})} A_r^{(\mathrm{s})}(v,c), \tag{5}$$

while the triplet excitation energies $\Omega_r^{(\mathrm{t})}$ are obtained from

$$\sum_{v',c'} D_{vc;v'c'}\, A_r^{(\mathrm{t})}(v',c') = \Omega_r^{(\mathrm{t})} A_r^{(\mathrm{t})}(v,c). \tag{6}$$

Here, $A_r^{(\mathrm{s})}(v,c)$ and $A_r^{(\mathrm{t})}(v,c)$ denote the singlet and triplet BSE amplitudes, respectively, representing the expansion coefficients of the electron–hole (exciton) wave functions (see Appendix):

$$\chi_r(\boldsymbol{r},\boldsymbol{r}') = -\sum_{v,c} A_r(v,c)\phi_c(\boldsymbol{r})\phi_v^*(\boldsymbol{r}'). \tag{7}$$

The matrix D represents a diagonal term minus a direct term, given by

$$D_{vc;v'c'} = (\varepsilon_c^{\mathrm{QP}} - \varepsilon_v^{\mathrm{QP}})\delta_{vv'}\delta_{cc'} - W_{vc;v'c'}, \tag{8}$$

where $W_{vc;v'c'}$ denote the matrix elements of the direct term, representing the screened electron–hole interaction, while $X_{vc;v'c'}$ in Eq. (5) denote the matrix elements of the exchange term. Therefore, in singlet excitation, the elements $W_{vc;v'c'} - 2X_{vc;v'c'}$ act as the exciton binding energy. Since the most important matrix element is the diagonal element between v = VBM and c = CBM, we will refer to the corresponding $W_{vc;vc} - 2X_{vc;vc}$ as the "superficial" exciton binding energy. The matrix

elements $W_{vc;v'c'}$ are the frequency integral of the dynamically screened Coulomb interaction $W(\boldsymbol{r},\boldsymbol{r}';\omega)$ multiplied by two energy denominator terms (see Appendix for the detailed derivation and a typo in the pioneering papers [71]),

$$W_{vc;v'c'} = \int d\boldsymbol{r}d\boldsymbol{r}'\phi_c^*(\boldsymbol{r})\phi_{c'}(\boldsymbol{r})\phi_v(\boldsymbol{r}')\phi_{v'}^*(\boldsymbol{r}')\,\frac{i}{2\pi}\int_{-\infty}^{\infty} d\omega W(\boldsymbol{r},\boldsymbol{r}';\omega)e^{-i\omega 0^+} \times\left[\frac{1}{\Omega_r-\omega-(\varepsilon_{c'}^{\mathrm{QP}}-\varepsilon_v^{\mathrm{QP}})+i0^+}+\frac{1}{\Omega_r+\omega-(\varepsilon_c^{\mathrm{QP}}-\varepsilon_{v'}^{\mathrm{QP}})+i0^+}\right], \tag{9}$$

where Ω_r denotes the photoabsorption energy (PAE) obtained as a final result. By decomposing $W(\boldsymbol{r},\boldsymbol{r}';\omega)$ as $1/|\boldsymbol{r}-\boldsymbol{r}'| + [\,W(\boldsymbol{r},\boldsymbol{r}';\omega) - 1/|\boldsymbol{r}-\boldsymbol{r}'|\,]$, Eq. (9) can be separated into two terms as

$$W_{vc;v'c'} = U_{vc;v'c'} + S_{vc;v'c'}, \tag{10}$$

where the matrix elements $U_{vc;v'c'}$ represent the bare Coulomb term,

$$U_{vc;v'c'} = \int \phi_c^*(\boldsymbol{r})\phi_{c'}(\boldsymbol{r})\,\frac{1}{|\boldsymbol{r}-\boldsymbol{r}'|}\,\phi_v(\boldsymbol{r}')\phi_{v'}^*(\boldsymbol{r}')\,d\boldsymbol{r}d\boldsymbol{r}', \tag{11}$$

and the matrix elements $S_{vc;v'c'}$ represent the remaining correlation term. In evaluating $S_{vc;v'c'}$, the generalize plasmon pole (GPP) model [44] is used to avoid the ω integration; see Appendix. On the other hand, the matrix elements $X_{vc;v'c'}$ of the exchange term are given by

$$X_{vc;v'c'} = \int \phi_c^*(\boldsymbol{r})\phi_v(\boldsymbol{r})\,\frac{1}{|\boldsymbol{r}-\boldsymbol{r}'|}\,\phi_{c'}(\boldsymbol{r}')\phi_{v'}^*(\boldsymbol{r}')\,d\boldsymbol{r}d\boldsymbol{r}'. \tag{12}$$

We evaluate $U_{vc;v'c'}$, $S_{vc;v'c'}$, and $X_{vc;v'c'}$ as well as $\langle\,\phi_n\,|\,\Sigma_x\,|\,\phi_n\,\rangle$ and $\langle\,\phi_n\,|\,\Sigma_c(\omega)\,|\,\phi_n\,\rangle$ in Eqs. (1) and (2) in Fourier space as (A.32)–(A.34) in Appendix; for $\langle\,\phi_n\,|\,\Sigma_x\,|\,\phi_n\,\rangle$ and $\langle\,\phi_n\,|\,\Sigma_c(\omega)\,|\,\phi_n\,\rangle$, see Ref. [44]. However, for the evaluation of $U_{vc;v'c'}$ and $X_{vc;v'c'}$ as well as $\langle\,\phi_n\,|\,\Sigma_x\,|\,\phi_n\,\rangle$, we exclude the fully on-site AO-only contributions, which are separately calculated in a single integral along the radial direction, as accurately as possible, using analytic integral forms of the Poisson equation for one-center problem. Finally, to obtain PAS, contributions from three mutually orthogonal polarization directions — (100), (010) and (001) — are averaged using the formula provided in Ref. [54]. We have utilized all these formulas in our previous studies [58–60].

The exchange terms $\langle\,\phi_n\,|\,\Sigma_x\,|\,\phi_n\,\rangle$ and $X_{vc;v'c'}$ and the bare Coulomb term $U_{vc;v'c'}$ are evaluated using approximately 88,000 $\boldsymbol{G}$ vectors, corresponding to a cutoff energy of 103.6 Ry. In contrast, the polarization function $P = -iGG$ and the correlation terms $\langle\,\phi_n\,|\,\Sigma_c(\omega)\,|\,\phi_n\,\rangle$ and $S_{vc;v'c'}$ are evaluated with approximately 4000 $\boldsymbol{G},\boldsymbol{G}'$ vectors, corresponding to a cutoff energy of 13.2 Ry. In solving the BSE, we include 50 empty levels along with all occupied valence levels. We confirmed that these parameters are sufficient to achieve convergence in the resulting QP and PAEs within 0.1 eV.

Lastly, we briefly comment on the tuning of the code within the hybrid MPI-OpenMP parallel architecture. The GW + BSE portion of TOMBO requires extensive computations, making performance optimization crucial. To reduce computational time, several techniques were implemented in this study. First, the conditional branches at the innermost loop nesting structure was removed and the computation sequence was adjusted to ensure continuous memory access. This change allowed for more efficient use of the SIMD arithmetic unit and cache memory in the CPU. Additionally, the data structure was modified so that intermediate data generated during computation is retained in memory rather than being written to a file, which reduced file I/O time. These efficiency improvements resulted in approximately a twofold speed-up. Furthermore, by minimizing the number of computing nodes used in each case, it became possible to run a large number of cases simultaneously.

3. Results

First, the optimized parameters of the tetragonal supercell, along with the resulting LDA energy gap $\Delta\varepsilon^{\mathrm{LDA}}$ and QP (GW) energy gap $\Delta\varepsilon^{\mathrm{QP}}$, are listed in Table 1. The QP energy gap of pure rutile is 3.34 eV, which is consistent with previous GW results of 3.3 eV [66,67], 3.34 eV [70], and 3.59 eV [72], as well as the experimental value of 3.3±0.5 eV [73]. For Zr doped rutile, both the LDA and QP energy gaps are nearly the same as those of pristine rutile. This finding aligns with a previous study [21] that indicated minimal changes in the LDA band structure due to the substitution of Zr, which is expected given that Zr and Ti are both group 4 elements. In contrast, all other systems doped with Mo, Zn, or Cd exhibit lower LDA and QP energy gaps. Our result for Mo doped rutile is consistent with the DFT-level spectra calculated by Soussi et al. [26].

Table 1
Optimized parameters of the tetragonal supercell and resulting LDA gap $\Delta\varepsilon^{\mathrm{LDA}}$ and QP (GW) energy gap $\Delta\varepsilon^{\mathrm{QP}}$.

System	$a=b$	c	$\Delta\varepsilon^{\mathrm{LDA}}$	$\Delta\varepsilon^{\mathrm{QP}}$
pure rutile	9.1453 Å	8.7767 Å	1.78 eV	3.34 eV
Zr@rutile	9.1623 Å	8.8197 Å	1.80 eV	3.39 eV
Mo@rutile	9.1654 Å	8.7718 Å	0.30 eV	0.97 eV
Zn@rutile	9.1499 Å	8.7958 Å	0.40 eV	1.08 eV
Cd@rutile	9.1801 Å	8.8269 Å	0.24 eV	0.810 eV
Zn+OV@rutile	9.1363 Å	8.8223 Å	1.78 eV	3.37 eV
Cd+OV@rutile	9.1449 Å	8.8639 Å	1.76 eV	3.39 eV

Next, the resulting singlet PAS are shown in Fig. 1. The low-energy regions of the PAS for (a) pure rutile, (c) Zr@rutile, and (e) Mo@rutile are magnified in the right panels (b), (d) and (f), respectively. For pure rutile (Fig. 1(a), (b)), the photoabsorption begins around 3 eV, which aligns well with the experimental evidence [74]. Although there is a side peak at approximately 3.75 eV and no peak around 8.5 eV in Fig. 1(b) in contrast to the previous GW + BSE calculations [70,75,76], the overall behavior is in good agreement with the experimental PAS [77]. Similarly, for Zr doped rutile (Fig. 1(c), (d)), the photoabsorption starting around 3 eV is consistent with the experimental absorption edge [19]. In the case of Mo (Fig. 1(e), (f)), the low-energy spikes at 1.5 eV and around 2 and 3 eV in the PAS of Fig. 1(f) may contribute to the long absorption tail and the observed red shift of the absorption edge by approximately 0.5 eV in the experimental photoabsorption spectra [23].

In contrast, for Zn and Cd, large peaks appear around 1 eV in Fig. 1(g) and (h). However, it is noteworthy that there is no such evidence in the experimental PAS, although small red shifts of 0.05–0.1 eV have been reported for the absorption edge in the experiments [27–30]. We found that this significant discrepancy arises because Zn and Cd impurity atoms must coexist with OV to compensate for the charge difference between Zn^{2+}/Cd^{2+} and Ti^{4+}. To address this, we introduced an OV in the vicinity of the Zn/Cd atom in the supercell and performed a full optimization of the system. The relaxed supercell parameters, along with the resulting LDA and GW energy gaps, are listed in the last two rows of Table 1. The LDA and GW energy gaps for these systems are clearly larger than those for systems without OV, suggesting the stability of the Zn/Cd-OV pair in rutile TiO_2. The singlet PAS for these systems are shown in Fig. 2. The low energy portions of the PAS for (a) Zn+OV@rutile and (c) Cd+OV@rutile are magnified in the right panels (b) and (d). As expected, the peaks around 1 eV have disappeared, and the overall behavior has become similar to that of pristine rutile. Now, the absorption intensity below 4 eV decreases smoothly toward zero, aligning with the experimental PAS [27–30]. The small red shift reported for the absorption edge may be attributed to an imperfect coexistence of Zn/Cd and OV. Specifically, this small red shift could be observed in the absorption edge if some Zn/Cd impurities without OV were also present in the sample.

4. Discussion

For pure rutile, we examined the convergence of results with respect to the supercell size. We performed GW + BSE calculations using several different supercells, ranging from 2 × 1 × 1 to 2 × 2 × 4,

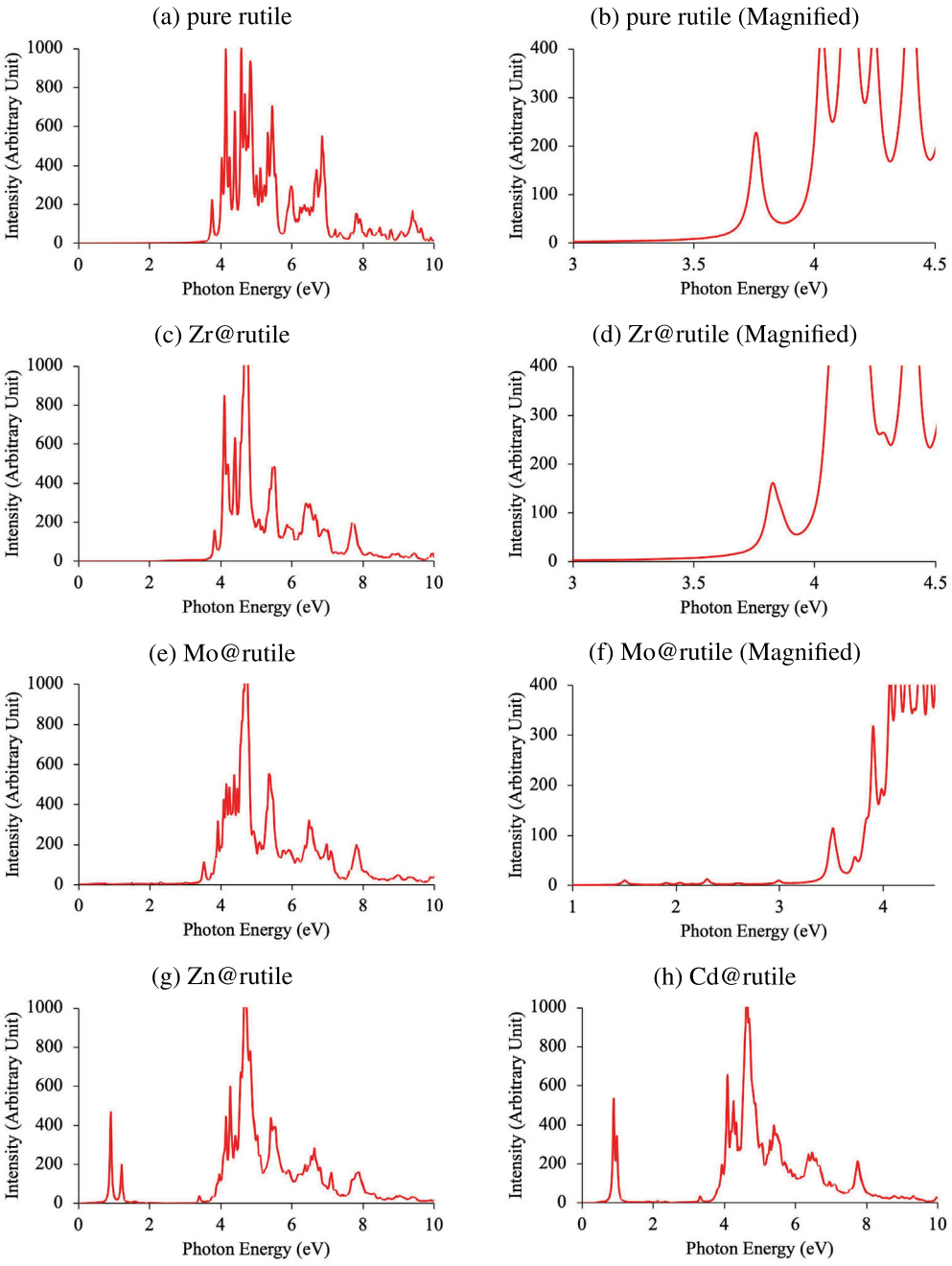

Fig. 1. Resulting PAS of (a), (b) pure rutile, (c), (d) Zr@rutile, (e), (f) Mo@rutile, (g) Zn@rutile, and (h) Cd@rutile. Panels (b), (d) and (f) are magnified plots of (a), (c) and (e).

while maintaining consistent cutoff energies and the number of levels as used in the 2 × 2 × 3 supercell. (Note that the 2 × 2 × 4 supercell utilized a slightly lower cutoff energy of 69.9 Ry for $\langle \phi_n | \Sigma_x | \phi_n \rangle$ and $U_{vc;v'c'}$ due to computing resource limitations.) The resulting LDA and QP energy gaps, along with the first three lower PAEs (i.e., the energy eigenvalues from the singlet Eq. (5) of the BSE), are shown in Table 2. As indicated in this table, both the energy gaps and PAEs approach certain values as the supercell size increases, although the changes are not so significant. This suggests that the 2 × 2 × 3 supercell is sufficient within the accuracy of 0.1 eV, yielding a QP (GW) energy gap $\Delta\varepsilon^{\mathrm{QP}}$ of approximately 3.3 eV.

In addition to this check, we also evaluated the GW calculation of the 6-atom primitive cell using $\boldsymbol{k}$-point sampling with various $\boldsymbol{k}$-point meshes, ranging from 2 × 1 × 1 to 3 × 3 × 6 for pure rutile. The resulting LDA and QP energy gaps are presented in Table 3. The dependence of the energy gaps on the $\boldsymbol{k}$-point grid is notably significant and scattered compared to their dependence on supercell size in Table 2. The convergence with respect to the $\boldsymbol{k}$-point mesh is slow, and the 3 × 3 × 6 mesh does not appear to be fully converged. Indeed, previous studies [67,70,72,75,76] have utilized 4 × 4 × 6 $\boldsymbol{k}$-points or more for better convergence. In our prior work [67] using the same TOMBO code with a 5 × 5 × 8 $\boldsymbol{k}$-point grid, we obtained a QP energy gap $\Delta\varepsilon^{\mathrm{QP}}$ of 3.30 eV.

Below, we will discuss the validity of using only the Γ-point in the GW + BSE approach in more detail. The primary condition for asserting the validity of this approach is that the Γ-point only GW calculation in the large supercell should reasonably reproduce the available experimental and theoretical band gaps. This criterion is essential for judging whether the Γ-point only GW + BSE approach is applicable in a supercell system. Next, we consider the specifics of

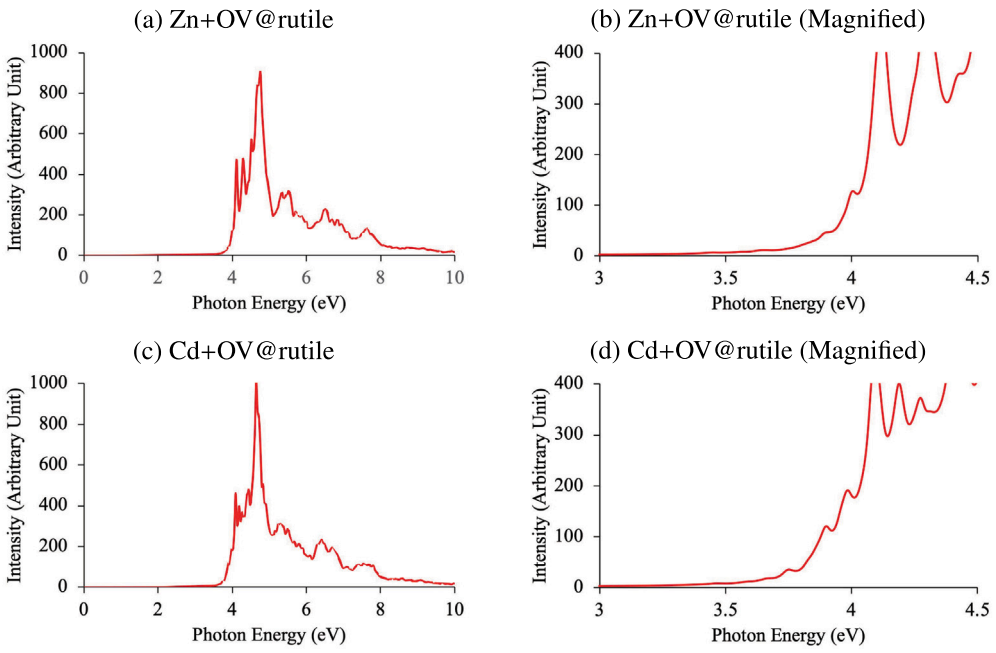

Fig. 2. Resulting PAS of (a), (b) Zn+OV@rutile and (c), (d) Cd+OV@rutile. Panels (b) and (d) are magnified plots of (a) and (c).

Table 2
Change in the LDA gap $\Delta\varepsilon^{\mathrm{LDA}}$, QP ($GW$) energy gap $\Delta\varepsilon^{\mathrm{QP}}$, and first three lower PAEs (i.e., the energy eigenvalues of the singlet Eq. (5) of the BSE) with respect to the supercell size.

Supercell	$\Delta\varepsilon^{\mathrm{LDA}}$ (eV)	$\Delta\varepsilon^{\mathrm{QP}}$ (eV)	PAEs (eV)		
$2\times1\times1$	1.46	2.92	2.85	2.92	3.00
$2\times1\times2$	1.57	3.31	3.28	3.37	3.37
$2\times1\times3$	1.74	3.49	3.47	3.61	3.80
$2\times1\times4$	1.72	3.24	3.22	3.22	3.35
$2\times2\times1$	1.61	3.42	3.23	3.25	3.25
$2\times2\times2$	1.61	3.21	3.17	3.20	3.21
$2\times2\times3$	1.78	3.34	3.32	3.37	3.37
$2\times2\times4$	1.77	3.29	3.18	3.18	3.18

Table 3
Change in the LDA gap $\Delta\varepsilon^{\mathrm{LDA}}$ and QP (GW) energy gap $\Delta\varepsilon^{\mathrm{QP}}$ (in units of eV) with respect to the $\boldsymbol{k}$-points.

$\boldsymbol{k}$-points	$\Delta\varepsilon^{\mathrm{LDA}}$	$\Delta\varepsilon^{\mathrm{QP}}$	$\boldsymbol{k}$-points	$\Delta\varepsilon^{\mathrm{LDA}}$	$\Delta\varepsilon^{\mathrm{QP}}$	$\boldsymbol{k}$-points	$\Delta\varepsilon^{\mathrm{LDA}}$	$\Delta\varepsilon^{\mathrm{QP}}$
$2\times1\times1$	1.61	3.40	$2\times2\times1$	1.67	3.70	$3\times3\times1$	1.45	3.77
$2\times1\times2$	1.83	3.87	$2\times2\times2$	1.87	4.09	$3\times3\times2$	1.82	4.06
$2\times1\times3$	1.52	3.10	$2\times2\times3$	1.52	2.91	$3\times3\times3$	1.45	3.14
$2\times1\times4$	1.73	3.48	$2\times2\times4$	1.72	3.45	$3\times3\times4$	1.63	3.38
$2\times1\times5$	1.68	3.26	$2\times2\times5$	1.72	3.36	$3\times3\times5$	1.69	3.34
$2\times1\times6$	1.73	3.52	$2\times2\times6$	1.74	3.45	$3\times3\times6$	1.70	3.38

Table 4
Diagonal elements between v = VBM and c = CBM of direct Coulomb term $U_{vc;vc}$, direct correlation term $S_{vc;vc}$, direct (screened Coulomb) term $W_{vc;vc} = U_{vc;vc} + S_{vc;vc}$, exchange term $X_{vc;vc}$, and "superficial" exciton binding energy $W_{vc;vc} - 2X_{vc;vc} = U_{vc;vc} + S_{vc;vc} - 2X_{vc;vc}$ in units of eV.

System	$U_{vc;vc}$	$S_{vc;vc}$	$W_{vc;vc}$	$X_{vc;vc}$	$W_{vc;vc} - 2X_{vc;vc}$
pure rutile	−0.0377	0.0212	−0.0165	0.0018	−0.0201
Zr@rutile	−0.0316	0.0190	−0.0126	0.0023	−0.0172
Mo@rutile	1.8773	−1.4117	0.4656	0.1395	0.1866
Zn@rutile	0.1880	−0.0687	0.1193	0.1253	−0.1313
Cd@rutile	0.2349	−0.0970	0.1379	0.0957	−0.0535
Zn+OV@rutile	−0.0629	0.0441	−0.0188	0.0036	−0.0260
Cd+OV@rutile	−0.0624	0.0442	−0.0182	0.0044	−0.0270

Table 5
First eight lower PAEs, i.e., the energy eigenvalues of the singlet Eq. (5) of the BSE.

System	PAEs (eV)							
pure rutile	3.32	3.37	3.37	3.57	3.64	3.64	3.65	3.65
Zr@rutile	3.36	3.37	3.41	3.59	3.60	3.62	3.63	3.65
Mo@rutile	0.71	0.75	1.32	1.42	1.44	1.46	1.50	1.54
Zn@rutile	0.91	1.08	1.10	1.21	1.53	1.54	1.54	1.58
Cd@rutile	0.808	0.89	0.98	1.01	1.28	1.42	1.50	1.53
Zn+OV@rutile	3.35	3.42	3.45	3.50	3.56	3.56	3.64	3.66
Cd+OV@rutile	3.36	3.41	3.45	3.48	3.55	3.58	3.60	3.64

the BSE calculation using only the Γ-point. In the singlet BSE (5), the most important matrix elements are the diagonal elements between v = VBM and c = CBM for the direct Coulomb term $U_{vc;vc}$ (Eq. (11)), the direct correlation term $S_{vc;vc}$ (Eq. (10)), and the exchange term $X_{vc;vc}$ (Eq. (12)). These values are summarized in Table 4. Additionally, the direct (screened Coulomb) term $W_{vc;vc} = U_{vc;vc} + S_{vc;vc}$, and the "superficial" exciton binding energy $W_{vc;vc} - 2X_{vc;vc} = U_{vc;vc} + S_{vc;vc} - 2X_{vc;vc}$ are presented in the fourth and sixth (last) columns of this table.

For the Mo@rutile system, $U_{vc;vc}$ is a large positive value, while $S_{vc;vc}$ is a moderate negative value. Consequently, the screened electron–hole interaction $W_{vc;vc} = U_{vc;vc} + S_{vc;vc}$ remains positive. On the other hand, $X_{vc;vc}$ is small and positive. As a result, the "superficial" exciton binding energy $W_{vc;vc} - 2X_{vc;vc}$ is also positive, making the VBM–CBM diagonal element of $D_{vc;vc} + 2X_{vc;vc}$ in the singlet Eq. (5) (i.e., "superficial" PAE) smaller than the QP energy gap $\Delta\varepsilon^{\mathrm{QP}} = \varepsilon_c^{\mathrm{QP}} - \varepsilon_v^{\mathrm{QP}}$. Indeed, as shown in Table 5, the lower PAEs, i.e., lower energy eigenvalues of the singlet Eq. (5), for Mo@rutile are smaller than the QP energy gap $\Delta\varepsilon^{\mathrm{QP}}$ presented in Table 1. The "real" exciton binding energy, which can be defined as $\Delta\varepsilon^{\mathrm{QP}}$– (the lowest PAE), is listed in Table 6. This value is 0.26 eV in the case of the Mo@rutile system. This explains the appearance of peaks at small PAEs in Fig. 1(f) for the Mo impurity case.

Conversely, for pure rutile, Zr@rutile, Zn+OV@rutile, and Cd+OV@rutile, $U_{vc;vc}$ is marginally negative, while $S_{vc;vc}$ is small but positive, and $X_{vc;vc}$ is very small and positive. Consequently, the screened electron–hole interaction $W_{vc;vc} = U_{vc;vc} + S_{vc;vc}$ and the "superficial" exciton binding energy $W_{vc;vc} - 2X_{vc;vc}$ are both marginally negative. However, the lowest PAE listed in Table 5 is at least slightly smaller than the QP energy gap $\Delta\varepsilon^{\mathrm{QP}}$ in Table 1. Therefore, as shown

Table 6
"real" exciton binding energy, i.e., $\Delta\varepsilon^{\mathrm{QP}}-$ (the lowest PAE).

System	$\Delta\varepsilon^{\mathrm{QP}}-$ (the lowest PAE) (eV)
pure rutile	0.02
Zr@rutile	0.03
Mo@rutile	0.26
Zn@rutile	0.17
Cd@rutile	0.002
Zn+OV@rutile	0.02
Cd+OV@rutile	0.03

in Table 6, the "real" exciton binding energy, $\Delta\varepsilon^{\mathrm{QP}}-$ (the lowest PAE), is positive, even if it is very small.

The Zn@rutile and Cd@rutile systems behave somewhere between these two extremes. As shown in Table 4, $U_{vc;vc}$ is a positive but small, while $S_{vc;vc}$ is marginally negative. Thus, the screened electron–hole interaction $W_{vc;vc}$ remains positive, although small. If we subtract $2X_{vc;vc}$ from this $W_{vc;vc}$, the resulting "superficial" exciton binding energy becomes marginally negative similar to the cases for pure rutile, Zr@rutile, Zn+OV@rutile, and Cd+OV@rutile. Similarly, as shown in Table 6, the "real" exciton binding energy becomes positive, although the value is quite small for Cd@rutile. However, the origin of the lower energy spikes in Fig. 1(g) and (h) is different from the VBE (v) and CBE (c) levels and related to the levels far away from the VBE and CBE. This is, of course, an exceptional case, due to the inherent chemical instability of these systems.

The marginally negative values of the screened electron–hole interaction $W_{vc;vc}$ may also arise when v and c correspond to the same $\boldsymbol{k}$-point in $\boldsymbol{k}$-point samplings. The vanishing $\boldsymbol{G} = 0$ component of $W_{vc;vc}$ is the reason for its potential negativity. Typically, the Fourier transform of the bare Coulomb interaction $v(\boldsymbol{G}) = 4\pi/\Omega|\boldsymbol{G}|^2$ (where Ω is the volume of the supercell) is set to a nonzero value at $\boldsymbol{G} = 0$ [78–80]. Then, in a plasmon pole model [44,81,82], the $\boldsymbol{G} = 0$ component of the screened electron–hole interaction $W_{vc;vc}$ automatically vanishes.

When we express $W_{vc;vc}$ as $W_{vc;vc} = U_{vc;vc} + S_{vc;vc}$ (see Eq. (10)), the $\boldsymbol{G} = 0$ component of $S_{vc;vc}$ in a plasmon pole model also vanishes for the same reason; see Appendix. The $\boldsymbol{G} = 0$ component of the bare Coulomb interaction $U_{vc;vc}$ must similarly vanish in the following reason. Inside the unit cell, the vv and cc charges in Eq. (11) are exactly equal to unity:

$$\int \phi_c^*(\boldsymbol{r})\phi_c(\boldsymbol{r})\,d\boldsymbol{r} \;=\; \int \phi_v(\boldsymbol{r})\phi_v^*(\boldsymbol{r})\,d\boldsymbol{r} \;=\; 1. \tag{13}$$

Considering their signs, the vv and cc charges are plus and minus one, respectively. Their images repeat across all unit cells, ensuring overall charge neutrality for the whole system. Therefore, the $\boldsymbol{G} = 0$ component of their Coulomb interaction $U_{vc;vc}$ must be set to zero. (In the Γ-point only calculation, if we sum up all cc charges independently of all vv charges over all unit cells, the Coulomb integral will obviously diverge. Instead, to take into account the excitonic effect correctly, we have to count not only the interaction between the cc and vv charges but also the interaction between cc and cc (or vv and vv) charges in different unit cells, at least in the $G = 0$ limit. Therefore, we can assume charge neutrality in this calculation. Note that this issue does not arise in $\boldsymbol{k}$-point sampling, because cc and vv charges are only assumed in the particular unit cell under consideration.) The $\boldsymbol{G} = 0$ component of the exchange term $X_{vc;vc}$ also vanishes, because

$$\int \phi_c^*(\boldsymbol{r})\phi_v(\boldsymbol{r})\,d\boldsymbol{r} \;=\; \int \phi_c(\boldsymbol{r}')\phi_v^*(\boldsymbol{r}')\,d\boldsymbol{r}' \;=\; 0 \tag{14}$$

clearly holds in the $\boldsymbol{G} = 0$ limit (see Appendix).

In the context of $\boldsymbol{k}$-point samplings, marginally negative values of the "superficial" exciton binding energy ($W_{vc;vc} - 2X_{vc;vc}$) can lead to a positive value for the "real" exciton binding energy ($\Delta\varepsilon^{\mathrm{QP}}-$ the lowest PAE) as follows. Consider, for example, the inclusion of the X-point alongside the Γ-point, assuming no mixing between different levels for simplicity. In this case, the singlet Eq. (5) becomes

$$\begin{bmatrix} D_{v_\Gamma c_\Gamma;v_\Gamma c_\Gamma} + 2X_{v_\Gamma c_\Gamma;v_\Gamma c_\Gamma} & -W_{v_\Gamma c_\Gamma;v_X c_X} + 2X_{v_\Gamma c_\Gamma;v_X c_X} \\ -W_{v_X c_X;v_\Gamma c_\Gamma} + 2X_{v_X c_X;v_\Gamma c_\Gamma} & D_{v_X c_X;v_X c_X} + 2X_{v_X c_X;v_X c_X} \end{bmatrix} \begin{bmatrix} A^{(\mathrm{s})}(v_\Gamma, c_\Gamma) \\ A^{(\mathrm{s})}(v_X, c_X) \end{bmatrix}$$
$$= \Omega_\pm^{(\mathrm{s})} \begin{bmatrix} A^{(\mathrm{s})}(v_\Gamma, c_\Gamma) \\ A^{(\mathrm{s})}(v_X, c_X) \end{bmatrix}. \tag{15}$$

If $D_{vc;vc} = \Delta\varepsilon^{\mathrm{QP}} - W_{vc;vc}$ and $X_{vc;vc}$ are independent of the Γ- and X-points (i.e., behave as constants), the secular equation can be expressed as

$$\left(\Delta\varepsilon^{\mathrm{QP}} - W_{vc;vc} + 2X_{vc;vc} - \Omega_\pm^{(\mathrm{s})}\right)^2 - \left|-W_{v_\Gamma c_\Gamma;v_X c_X} + 2X_{v_\Gamma c_\Gamma;v_X c_X}\right|^2 = 0, \tag{16}$$

which yields the following ± solutions:

$$\Omega_\pm^{(\mathrm{s})} = \Delta\varepsilon^{\mathrm{QP}} - W_{vc;vc} + 2X_{vc;vc} \pm \left|-W_{v_\Gamma c_\Gamma;v_X c_X} + 2X_{v_\Gamma c_\Gamma;v_X c_X}\right| \tag{17}$$

Therefore, when $W_{vc;vc}$ is marginally negative, the − solution can offset the negative "superficial" exciton binding energy, shifting the "real" exciton binding energy to a positive value. This effect becomes more pronounced with the inclusion of additional $\boldsymbol{k}$-points, of course.

Now, we demonstrate that a similar explanation applies to supercell calculations without $\boldsymbol{k}$-point samplings. Assume that a unit cell (either primitive or supercell) is doubled in one direction, and the number of levels at the Γ-point is also doubled. If we ignore all the v-v' and c-c' interlevel interactions except for the interaction between CBM (0) and CBM+1 (1), the singlet Eq. (5) becomes

$$\begin{bmatrix} D_{vc_0;vc_0} + 2X_{vc_0;vc_0} & -W_{vc_0;vc_1} + 2X_{vc_0;vc_1} \\ -W_{vc_1;vc_0} + 2X_{vc_1;vc_0} & D_{vc_1;vc_1} + 2X_{vc_1;vc_1} \end{bmatrix} \begin{bmatrix} A^{(\mathrm{s})}(v, c_0) \\ A^{(\mathrm{s})}(v, c_1) \end{bmatrix}$$
$$= \Omega_\pm^{(\mathrm{s})} \begin{bmatrix} A^{(\mathrm{s})}(v, c_0) \\ A^{(\mathrm{s})}(v, c_1) \end{bmatrix}. \tag{18}$$

Again, if $D_{vc;vc} = \Delta\varepsilon^{\mathrm{QP}} - W_{vc;vc}$ and $X_{vc;vc}$ are independent of c_0 and c_1, and behave as constants, the secular equation is obtained as

$$\left(\Delta\varepsilon^{\mathrm{QP}} - W_{vc;vc} + 2X_{vc;vc} - \Omega_\pm^{(\mathrm{s})}\right)^2 - \left|-W_{vc_0;vc_1} + 2X_{vc_0;vc_1}\right|^2 = 0, \tag{19}$$

which results in the following ± solutions:

$$\Omega_\pm^{(\mathrm{s})} = \Delta\varepsilon^{\mathrm{QP}} - W_{vc;vc} + 2X_{vc;vc} \pm \left|-W_{vc_0;vc_1} + 2X_{vc_0;vc_1}\right|. \tag{20}$$

Thus, even if the screened electron–hole interaction $W_{vc;vc}$ is marginally negative, the − solution can compensate for the negative "superficial" exciton binding energy, potentially shifting the "real" exciton binding energy ($\Delta\varepsilon^{\mathrm{QP}} - \Omega_-^{(\mathrm{s})}$) to a positive value. This effect becomes more prominent with larger supercell. Therefore, the marginally negative values of $W_{vc;vc}$ and the "superficial" exciton binding energy need not be a major concern.

We present the resulting exciton wave functions (EWFs) for Mo@rutile at PAEs of 0.71 eV and 1.54 eV in Fig. 3. The position of the hole is fixed near the impurity atom. As illustrated in the figures, the EWFs are clearly localized around the impurity. This supercell calculation can be likened to using some $\boldsymbol{k}$-point mesh in the calculation of the six-atom primitive unit cell. If this analogy holds, similar EWFs would also emerge in such $\boldsymbol{k}$-point samplings. In general, to fully confine EWFs within an $n_1 \times n_2 \times n_3$ supercell, it would be necessary to either increase the supercell size or the number of the $\boldsymbol{k}$-points in the primitive unit cell, both of which are computationally demanding tasks. The spatial extension of EWFs is related to the "real" exciton binding energy. For Mo@rutile, the "real" exciton binding energy $\Delta\varepsilon^{\mathrm{QP}}-$ (the lowest PAE) = 0.26 eV (see Table 6), which is reasonably large. This value is further greater than the positive "superficial" exciton binding energy $W_{vc;vc} - 2X_{vc;vc} = 0.19$ eV in Table 4, indicating that it corresponds to a Frenkel exciton.

On the other hand, for pure@rutile, Zr@rutile, Zn+OV@rutile, and Cd+OV@rutile, the "real" exciton binding energies ($\Delta\varepsilon^{\mathrm{QP}}-$ the lowest PAE) listed in Table 6 are very small. These values fall well below the accuracy threshold of the GW + BSE calculation. Therefore, we can reasonably expect that there is no issue with depicting the PAS of these systems using only the Γ-point calculation, even though the

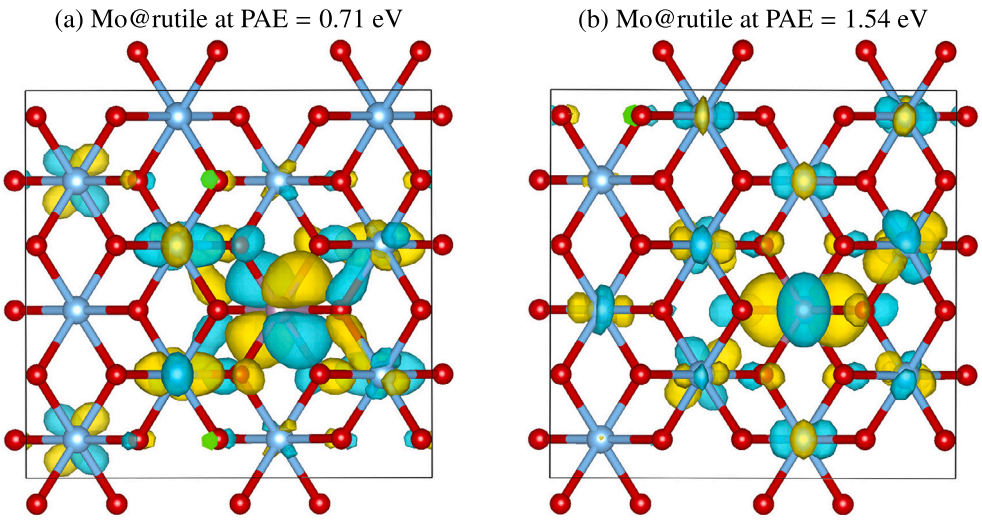

Fig. 3. Exciton wave functions (EWFs) of (a) Mo@rutile at PAE = 0.71 eV and (b) Mo@rutile at PAE = 1.54 eV. The position of hole is fixed at the vicinity of the impurity atom. Small sky blue, purple and red balls represent, respectively, Ti, Mo, and O atoms. Yellow and blue regions correspond, respectively, to plus and minus sign of the EWF. (For interpretation of the references to color in this figure legend, the reader is referred to the web version of this article.)

EWF may correspond to a widely spread Wannier exciton that cannot be fully confined within the supercell. A similar scenario would arise in primitive cell calculations using $\boldsymbol{k}$-point sampling. When the "real" exciton binding energy is smaller than the error bar of the GW + BSE calculation using $n_1 \times n_2 \times n_3$ $\boldsymbol{k}$-points, one can still accurately depict the PAS in $\boldsymbol{k}$-point sampling, even if the EWF is not confined within the unfolded $n_1 \times n_2 \times n_3$ supercell. According to Sham and Rice [83], this situation relates to the effective-mass equation for the Wannier exciton and corresponds to a weak electron–hole interaction. It is crucial to confirm that the "real" exciton binding energy ($\Delta\varepsilon^{\mathrm{QP}}$– the lowest PAE) is positive in both the Γ-point only BSE calculation and the BSE calculation utilizing $\boldsymbol{k}$-point sampling. Even if this value is exceptionally small, we can still compute the PAS reliably.

Finally, we would like to comment on the calculations involving magnetic impurities. We attempted to calculate the PAS of Cr@rutile and Ru@rutile but encountered difficulties due to the emergence of negative PAEs in the solution of Eq. (5) of the BSE. This failure is likely attributed to our neglect of spin polarization effects for Cr and Ru. Previous DFT studies [31,84,85] have highlighted the significance of spin polarization effects for these impurities. Therefore, the GW + BSE calculation for magnetic impurities will be addressed in future work.

5. Conclusion

We have employed the Γ-point only GW + BSE approach on a 72 (or 71) atom supercell to obtain the quasiparticle (QP) energy gaps and photoabsorption spectra (PAS) of pure rutile TiO_2 and those doped with nonmagnetic transition metal (Zr, Mo, Zn, Cd) impurities. The full ω integration was performed at the GW level, while the generalized plasmon pole (GPP) model was utilized at the BSE level. In Appendix, we identified a typo in the key expression of the screened electron–hole interaction $W_{vc;v'c'}$ in the BSE in the pioneering papers [71]. During our calculations, we found that Zn and Cd impurities should coexist with oxygen vacancies (OVs), as Zn^{2+} and Cd^{2+} are unstable at the Ti^{4+} substitutional site in TiO_2 without OVs. Among the systems studied, Mo, Zn, or Cd doped rutile TiO_2 demonstrate visible light absorbance and may exhibit catalytic activity under visible light. The resulting QP energies and PAS align roughly well with available experimental and theoretical data. We thoroughly discussed the validity of our approach and summarized the necessary conditions for the applicability of using only the Γ-point in the GW + BSE framework as follows: First, the Γ-point only GW calculation in the assumed supercell should reasonably reproduce the available experimental and theoretical band gaps. Second, the "superficial" exciton binding energy — i.e., the diagonal element of $W_{vc;vc} - 2X_{vc;vc}$ between v = VBM and c = CBM — must be positive or marginally negative. Third, physically, the "real" exciton binding energy ($\Delta\varepsilon^{\mathrm{QP}}$– the lowest PAE) should be positive, even if it is exceptionally small. The Γ-point only GW + BSE approach can effectively handle a wide range of periodic systems, including those with impurities and so on, while saving computational time.

CRediT authorship contribution statement

Kaoru Ohno: Writing – original draft, Validation, Software, Methodology, Investigation, Funding acquisition, Formal analysis. **Ryoji Sahara:** Writing – review & editing, Validation, Resources, Project administration, Investigation, Formal analysis. **Takeshi Nanri:** Writing – original draft, Software, Resources, Methodology. **Yoshiyuki Kawazoe:** Writing – review & editing, Validation, Project administration, Funding acquisition, Conceptualization.

Declaration of competing interest

The authors declare the following financial interests/personal relationships which may be considered as potential competing interests: Kaoru Ohno reports financial support was provided by Japan Society for the Promotion of Science. Yoshiyuki Kawazoe reports financial support was provided by Air Force Asian Office of Aerospace Research and Development. If there are other authors, they declare that they have no known competing financial interests or personal relationships that could have appeared to influence the work reported in this paper.

Acknowledgments

In this study, we utilized supercomputers at the Research Institute for Information Technology in Kyushu University (supported by the JHPCN project No.: jh240026), the Institute for Materials Research (IMR) in Tohoku University (Subject Nos.: 2211SC0501 and 2308SC0216), and the Institute for Solid State Physics in the University of Tokyo. One of the authors (K.O.) received support from the Japan Society for the Promotion of Science (JSPS) through KAKENHI Grants-in-Aid for Scientific Research B (Grant Nos. 21H01877 and 23K21094). The authors would like to thank Dr. Ruth Pachter from the Air Force Research Laboratory for suggesting this study and providing valuable insights. This work was also partially supported by the Asian Office of Aerospace Research and Development (AOARD) under project number

FA2386-22-1-4011. Y.K. acknowledges support from (i) the National Science, Research and Innovation Fund (NSRF) (NRIIS Project Number 90465), (ii) Thailand Science Research and Innovation (TSRI), and (iii) Suranaree University of Technology (SUT).

Appendix. Derivation of $W_{vc;v'c'}$

One-particle and two-particle Green's functions are defined, respectively, as [86]

$$G(x_1,x_2) = -i\langle \Phi_G^N \,|\, T[\psi(x_1)\psi^\dagger(x_2)] \,|\, \Psi_G^N \rangle, \tag{A.1}$$

$$G(x_1,x_2;x_1',x_2') = (-i)^2\langle \Phi_G^N \,|\, T[\psi(x_1)\psi(x_2)\psi^\dagger(x_2')\psi^\dagger(x_1')] \,|\, \Psi_G^N \rangle, \tag{A.2}$$

where T means the time ordered product; x_i and x_i' are the 4-vectors $(\boldsymbol{r}_i,t_i)$ and $(\boldsymbol{r}_i',t_i')$; $\psi(x)$ and $\psi^\dagger(x)$ represent the annihilation and creation operators in the Heisenberg representation. The two-particle correlation function is defined as

$$L(x_1,x_2;x_1',x_2') = -G(x_1,x_2;x_1',x_2') + G(x_1,x_1')G(x_2,x_2'), \tag{A.3}$$

which excludes completely disconnected diagrams from the two-particle Green's function. It satisfies the Bethe–Salpeter equation (BSE)

$$\begin{aligned} L(x_1,x_2;x_1',x_2') &= G(x_1,x_2')G(x_2,x_1') \\ &\quad + \int G(x_1,x_3)\Xi(x_3,x_4;x_3',x_4')G(x_3',x_1') \\ &\quad \times L(x_4',x_2;x_4,x_2')dx_3dx_3'dx_4dx_4'. \end{aligned} \tag{A.4}$$

From the GW self-energy Σ, the kernel $\Xi = \delta\Sigma/\delta G$ is

$$\begin{aligned} \Xi(x_3,x_4;x_3',x_4') &= -\,i\delta^4(x_3-x_3')\delta^4(x_4-x_4'^{+})v(x_3,x_4) \\ &\quad +\, i\delta^4(x_3-x_4')\delta^4(x_3'^{+}-x_4)W'(x_3,x_3'), \end{aligned} \tag{A.5}$$

where $v(x_3,x_4) = \delta(t_3-t_4)/|\boldsymbol{r}_3-\boldsymbol{r}_4|$ is the exchange term coming from the functional derivative of the Hartree term of the self-energy and $W'(x_3,x_3')$ is the direct term coming from the functional derivative of the exchange–correlation component of the self-energy. W' includes the second exchange term $G\delta W/\delta G \propto GWWG$ [58,60], but this term is usually ignored. Then, W' reduces to the dynamically screened Coulomb interaction W.

In cases where $t_1,\ t_1' \lesssim t_2,\ t_2'$ hold, the two-particle Green's function (A.2) becomes

$$\begin{aligned} &G(x_1,x_2;x_1',x_2') \\ &= -\,\langle \Phi_G^N \,|\, T[\psi(x_1)\psi^\dagger(x_1')]T[\psi(x_2)\psi^\dagger(x_2')] \,|\, \Psi_G^N \rangle\theta(\min(t_1,t_1') - \max(t_2,t_2')) \\ &\quad -\,\langle \Phi_G^N \,|\, T[\psi(x_2)\psi^\dagger(x_2')]T[\psi(x_1)\psi^\dagger(x_1')] \,|\, \Psi_G^N \rangle\theta(\min(t_2,t_2') - \max(t_1,t_1')). \end{aligned} \tag{A.6}$$

By inserting the complete set condition $\sum_S |\,\Psi_S^N\rangle\langle\Psi_S^N\,| = 1$ for the N-electron intermediate states $|\,\Psi_S^N\rangle$, which represent configurations with one particle and one hole (i.e., an exciton) excited from the ground state, in between two T products, the $\langle \Phi_G^N \,|\, ... \,|\, \Psi_G^N \rangle$ terms in Eq. (A.6) become

$$\sum_S \langle \Psi_G^N \,|\, T[\psi(x_1)\psi^\dagger(x_1')] \,|\, \Psi_S^N \rangle\langle \Psi_S^N \,|\, T[\psi(x_2)\psi^\dagger(x_2')] \,|\, \Psi_G^N \rangle, \tag{A.7a}$$

$$\sum_S \langle \Psi_G^N \,|\, T[\psi(x_2)\psi^\dagger(x_2')] \,|\, \Psi_S^N \rangle\langle \Psi_S^N \,|\, T[\psi(x_1)\psi^\dagger(x_1')] \,|\, \Psi_G^N \rangle. \tag{A.7b}$$

Following Strinati [51], we introduce the averaged and difference times as $t^1 = (t_1+t_1')/2$, $t^2 = (t_2+t_2')/2$, $\tau_1 = t_1 - t_1'$, and $\tau_2 = t_2 - t_2'$. From

$$\begin{aligned} &\langle \Psi_G^N \,|\, T[\psi(x_1)\psi^\dagger(x_1')] \,|\, \Psi_S^N \rangle = \big[\,\langle \Psi_G^N \,|\, \psi(\boldsymbol{r}_1)e^{-i\mathcal{H}\tau_1}\psi^\dagger(\boldsymbol{r}_1') \,|\, \Psi_S^N \rangle\theta(\tau_1) \\ &- \langle \Psi_G^N \,|\, \psi^\dagger(\boldsymbol{r}_1')e^{i\mathcal{H}\tau_1}\psi(\boldsymbol{r}_1) \,|\, \Psi_S^N \rangle\theta(-\tau_1)\,\big]\, e^{i[(E_G-E_S)t^1+(E_G+E_S)|\tau_1|/2]} \\ &= \chi_S(\boldsymbol{r}_1,\boldsymbol{r}_1';\tau_1)e^{i(E_G-E_S)t^1}, \end{aligned} \tag{A.8a}$$

$$\begin{aligned} &\langle \Psi_S^N \,|\, T[\psi(x_2)\psi^\dagger(x_2')] \,|\, \Psi_G^N \rangle = \big[\,\langle \Psi_S^N \,|\, \psi(\boldsymbol{r}_2)e^{-i\mathcal{H}\tau_2}\psi^\dagger(\boldsymbol{r}_2') \,|\, \Psi_G^N \rangle\theta(\tau_2) \\ &- \langle \Psi_S^N \,|\, \psi^\dagger(\boldsymbol{r}_2')e^{i\mathcal{H}\tau_2}\psi(\boldsymbol{r}_2) \,|\, \Psi_G^N \rangle\theta(-\tau_2)\,\big]\, \varepsilon^{i[(E_S-E_G)t^2+(E_G+E_S)|\tau_2|/2]} \\ &= \widetilde{\chi}_S(\boldsymbol{r}_2,\boldsymbol{r}_2';\tau_2)e^{i(E_S-E_G)t^2}, \end{aligned} \tag{A.8b}$$

Eqs. (A.7a) and (A.7b) become $\sum_S \chi_S(\boldsymbol{r}_1,\boldsymbol{r}_1';\tau_1)\widetilde{\chi}_S(\boldsymbol{r}_2,\boldsymbol{r}_2';\tau_2)\, e^{-i(E_S-E_G)(t^1-t^2)}$ and $\sum_S \widetilde{\chi}_S(\boldsymbol{r}_1,\boldsymbol{r}_1';\tau_1)\chi_S(\boldsymbol{r}_2,\boldsymbol{r}_2';\tau_2)e^{i(E_S-E_G)(t^1-t^2)}$, respectively.

Noting that $\min(t_1,t_1') = t^1 - |\tau_1|/2$ and $\max(t_2,t_2') = t^2 + |\tau_2|/2$, we find $\theta(\min(t_1,t_1') - \max(t_2,t_2')) = \theta(t^1 - t^2 - |\tau_1|/2 - |\tau_2|/2)$. Similarly, we have $\theta(\min(t_2,t_2') - \max(t_1,t_1')) = \theta(t^2 - t^1 - |\tau_1|/2 - |\tau_2|/2)$. In the limit $\tau_2 \to -0^+$, both t^2 and t_2' become $t^2, t_2' \to t_2$. Then, the time Fourier transformation of the two-particle Green's function (A.6) from t_2 to ω can be calculated as

$$\begin{aligned} &\int_{-\infty}^{\infty} e^{i(E_S-E_G)(t^2-t^1)}\,\theta(t^1-t^2-|\tau_1|/2-|\tau_2|/2)\,e^{-i\omega t_2}dt_2 \\ &= \int_{-\infty}^{\infty} e^{i(E_S-E_G)(t_2-t^1)-i\omega t_2}\,\theta(t^1-t_2-|\tau_1|/2)\,dt_2 \\ &= \int_{-\infty}^{t^1-|\tau_1|/2} e^{i\{(E_S-E_G)-\omega-i0^+\}t_2}dt_2\, e^{-i(E_S-E_G)t^1} \\ &= -i\frac{e^{i\{(E_S-E_G)-\omega\}(t^1-|\tau_1|/2)}}{(E_S-E_G)-\omega-i0^+}e^{-i(E_S-E_G)t^1} \\ &= i\frac{e^{-i\omega t^1}e^{-i(E_S-E_G)|\tau_1|/2}e^{i\omega|\tau_1|/2}}{\omega-(E_S-E_G)+i0^+}, \end{aligned} \tag{A.9a}$$

$$\begin{aligned} &\int_{-\infty}^{\infty} e^{i(E_S-E_G)(t^1-t^2)}\,\theta(t^2-t^1-|\tau_1|/2-|\tau_2|/2)\,e^{-i\omega t_2}dt_2 \\ &= \int_{-\infty}^{\infty} e^{i(E_S-E_G)(t^1-t_2)-i\omega t_2}\,\theta(t_2-t^1-|\tau_1|/2)\,dt_2 \\ &= \int_{t^1+|\tau_1|/2}^{\infty} e^{i\{-(E_S-E_G)-\omega+i0^+\}t_2}dt_2\, e^{i(E_S-E_G)t^1} \\ &= -i\frac{e^{i\{-(E_S-E_G)-\omega\}(t^1+|\tau_1|/2)}}{(E_S-E_G)+\omega-i0^+}e^{i(E_S-E_G)t^1} \\ &= -i\frac{e^{-i\omega t^1}e^{-i(E_S-E_G)|\tau_1|/2}e^{-i\omega|\tau_1|/2}}{\omega+(E_S-E_G)-i0^+}. \end{aligned} \tag{A.9b}$$

Thus, we have [51]

$$\begin{aligned} &L(\boldsymbol{r}_1,t_1,\boldsymbol{r}_2;\boldsymbol{r}_1',t_1-\tau_1,\boldsymbol{r}_2',\omega) \\ &\equiv -\int_{-\infty}^{\infty} L(\boldsymbol{r}_1,t_1,\boldsymbol{r}_2,t_2;\boldsymbol{r}_1',t_1-\tau_1,t_2,\boldsymbol{r}_2',t_2+0^+)e^{-i\omega t_2}dt_2 \\ &= -\,ie^{-i\omega(t^1-|\tau_1|/2)}\sum_S \frac{\chi_S(\boldsymbol{r}_1,\boldsymbol{r}_1';\tau_1)\widetilde{\chi}_S(\boldsymbol{r}_2,\boldsymbol{r}_2';-0^+)}{\omega-(E_S-E_G)+i0^+}e^{-i(E_S-E_G)|\tau_1|/2} \\ &\quad + ie^{-i\omega(t^1+|\tau_1|/2)}\sum_S \frac{\widetilde{\chi}_S(\boldsymbol{r}_1,\boldsymbol{r}_1';\tau_1)\chi_S(\boldsymbol{r}_2,\boldsymbol{r}_2';-0^+)}{\omega+(E_S-E_G)-i0^+}e^{-i(E_S-E_G)|\tau_1|/2}. \end{aligned} \tag{A.10}$$

Eq. (A.10) is still an exact expression without introducing any approximation. The first term on the right-hand side comprises the positive energy terms associated with exciton creations and the second term encompasses the negative energy terms linked to exciton recombinations. In this context, ω represents the photon energy, which is positive and can be approximated as being close to some resonant energy $\Omega_r = E_r - E_G$. As the photon energy approaches this resonant condition, one of the positive energy terms becomes dominant due to its denominator nearing zero. This allows us to neglect the negative energy terms, i.e., the second term of Eq. (A.10), and rewrite Eq. (A.10) as

$$\begin{aligned} &L(\boldsymbol{r}_1,t_1,\boldsymbol{r}_2;\boldsymbol{r}_1',t_1-\tau_1,\boldsymbol{r}_2',\omega) \simeq -\,ie^{-i\omega t^1}\frac{1}{\omega-\Omega_r+i0^+} \\ &\quad\times \sum_S \bar{\chi}_S(\boldsymbol{r}_1,\boldsymbol{r}_1';\tau_1)\bar{\widetilde{\chi}}_S(\boldsymbol{r}_2,\boldsymbol{r}_2';-0^+). \end{aligned} \tag{A.11}$$

Here, we put $\Omega_r = E_r - E_G$, and the functions with bar $\bar{\chi}_S(\boldsymbol{r}_1,\boldsymbol{r}_1';\tau_1)$, $\bar{\widetilde{\chi}}_S(\boldsymbol{r}_2,\boldsymbol{r}_2';\tau_2)$ are $\chi_S(\boldsymbol{r}_1,\boldsymbol{r}_1';\tau_1)$, $\widetilde{\chi}_S(\boldsymbol{r}_2,\boldsymbol{r}_2';\tau_2)$ with the excitation energy $E_S - E_G$ replaced by ω in Eqs. (A.8) and (A.12) (below).

According to Strinati [51], the particle–hole amplitudes $\chi_S(\boldsymbol{r}_1,\boldsymbol{r}_1';\tau_1)$ and $\widetilde{\chi}_S(\boldsymbol{r}_2,\boldsymbol{r}_2';\tau_2)$ are derived from their definition (A.8) by expanding the field operators in terms of the single-particle wave functions

$\phi_c(\boldsymbol{r})$ and $\phi_v(\boldsymbol{r})$ (by noting that $e^{-iH\tau_j}$ and $e^{iH\tau_j}$ in Eq. (A.8) become $e^{-i(E_G+\varepsilon_c^{\rm QP})\tau_j}$ and $e^{i(E_G-\varepsilon_v^{\rm QP})\tau_j}$, respectively, for both $j=1,2$) as

$$\chi_S(\boldsymbol{r}_1,\boldsymbol{r}_1';\tau_1) = -e^{i(E_S-E_G)|\tau_1|/2}\sum_{v,c} A_S(v,c)\phi_c(\boldsymbol{r}_1)\phi_v^*(\boldsymbol{r}_1') \times\left[\theta(\tau_1)e^{-i\varepsilon_c^{\rm QP}\tau_1}+\theta(-\tau_1)e^{-i\varepsilon_v^{\rm QP}\tau_1}\right], \tag{A.12a}$$

$$\widetilde{\chi}_S(\boldsymbol{r}_2,\boldsymbol{r}_2';\tau_2) = -e^{i(E_S-E_G)|\tau_2|/2}\sum_{v,c} A_S^*(v,c)\phi_v(\boldsymbol{r}_2)\phi_c^*(\boldsymbol{r}_2') \times\left[\theta(\tau_2)e^{-i\varepsilon_c^{\rm QP}\tau_2}+\theta(-\tau_2)e^{-i\varepsilon_v^{\rm QP}\tau_2}\right], \tag{A.12b}$$

where v and c stand for valence and conduction QP levels, respectively, and $e_v^{\rm QP}$ and $\varepsilon_c^{\rm QP}$ denote the corresponding QP energies. This corresponds to the Tamm–Dancoff approximation, neglecting the terms, where $A_S(v,c)$ is replaced by $B_S(v,c)$, and c and v are interchanged in Eq. (A.12) [57]. Multiplying Eq. (A.12b) with $\tau_2=-0^+$ by

$$\chi_r(\boldsymbol{r}_2',\boldsymbol{r}_2;-0^+) = -\sum_{v',c'} A_r(v',c')\phi_{c'}(\boldsymbol{r}_2')\phi_{v'}^*(\boldsymbol{r}_2), \tag{A.13}$$

integrating it with respect to $\boldsymbol{r}_2$ and $\boldsymbol{r}_2'$, and using $\int\phi_c^*(\boldsymbol{r}_2)\phi_{c'}(\boldsymbol{r}_2)d\boldsymbol{r}_2=\delta_{cc'}$ and $\int\phi_v(\boldsymbol{r}_2)\phi_{v'}^*(\boldsymbol{r}_2)d\boldsymbol{r}_2=\delta_{vv'}$, we have the orthonormality relation

$$\int\chi_r(\boldsymbol{r}_2,\boldsymbol{r}_2';-0^+)\widetilde{\chi}_S(\boldsymbol{r}_2,\boldsymbol{r}_2';-0^+)d\boldsymbol{r}_2d\boldsymbol{r}_2' = \sum_{v,c}A_r(v,c)A_S^*(v,c)=\delta_{rS}. \tag{A.14}$$

To obtain the matrix form of the BSE, we will finally multiply the BSE (A.4) by $\phi_c^*(\boldsymbol{r}_1)\phi_v(\boldsymbol{r}_1')$ and integrate with respect to $\boldsymbol{r}_1$ and $\boldsymbol{r}_1'$. Keeping this in mind, we start by considering the first term on the right-hand side of the BSE (A.4), $G(x_1,x_2')G(x_2,x_1')$, in the limit $\tau_1,\tau_2\to-0^+$ ($t_i=t_i'-0^+$ for $i=1,2$). Keeping only the contributions where $\boldsymbol{r}_1$ corresponds to the conduction band (c) and $\boldsymbol{r}_1'$ corresponds to the valence band (v), we have

$$\begin{aligned}&G(t_1-t_2)G(t_2-t_1)\\ &=\sum_c\int\frac{d\omega_1}{2\pi}\frac{e^{-i\omega_1(t_1-t_2)}}{\omega_1-\varepsilon_c^{\rm QP}+i0^+}\sum_v\int\frac{d\omega_2}{2\pi}\frac{e^{-i\omega_2(t_2-t_1)}}{\omega_2-\varepsilon_v^{\rm QP}-i0^+}\\ &=\sum_{c,v}\int\frac{d\omega_1d\omega_2}{(2\pi)^2}\frac{e^{-i(\omega_1-\omega_2)t_1}e^{i(\omega_1-\omega_2)t_2}}{(\omega_1-\varepsilon_c^{\rm QP}+i0^+)(\omega_2-\varepsilon_v^{\rm QP}-i0^+)}.\end{aligned} \tag{A.15}$$

Fourier transforming this from t_2 to ω (note that the t_2 integration becomes $2\pi\delta(\omega_1-\omega_2-\omega)$, yielding $\omega_2=\omega_1-\omega$), multiplying it by Eq. (A.13), and integrating it with respect to $\boldsymbol{r}_2$ and $\boldsymbol{r}_2'$, we obtain

$$\begin{aligned}&\int_{-\infty}^{\infty}dt_2e^{-i\omega t_2}\int G(x_1,x_2')G(x_2,x_1')\chi_r(\boldsymbol{r}_2',\boldsymbol{r}_2;-0^+)d\boldsymbol{r}_2d\boldsymbol{r}_2'\\ &=-e^{-i\omega t_1}\sum_{c,v}\int\frac{d\omega_1}{2\pi}\frac{1}{(\omega_1-\varepsilon_c^{\rm QP}+i0^+)(\omega_1-\omega-\varepsilon_v^{\rm QP}-i0^+)}\\ &\quad\times A_r(v,c)\phi_c(\boldsymbol{r}_1)\phi_v^*(\boldsymbol{r}_1')\\ &=\sum_{d,c}\frac{-ie^{-i\omega t_1}}{\omega-\left(\varepsilon_c^{\rm QP}-\varepsilon_v^{\rm QP}\right)}A_r(v,c)\phi_c(\boldsymbol{r}_1)\phi_v^*(\boldsymbol{r}_1').\end{aligned} \tag{A.16}$$

We have to further multiply this by -1, because $L(\omega)$ in Eq. (A.10) is defined with a minus sign. However, we multiply the entire BSE (A.4) by an additional factor -1. Then, this -1 factor is absorbed in the definition of $L(\omega)$ on the left-hand side and in the second term of the right-hand side of the BSE. Thus, the explicit multiplication by -1 is only necessary for the first term on the right-hand side.

Also, for the left-hand side of the BSE, we multiply $L(\omega)$ (i.e., Eq. (A.11) with Eq. (A.12a), replacing E_S-E_G with ω) by Eq. (A.13) and integrate over $\boldsymbol{r}_2$ and $\boldsymbol{r}_2'$. This gives us, from Eq. (A.14),

$$-\left(\frac{-ie^{-i\omega t^1}e^{i\omega|\tau_1|/2}}{\omega-\Omega_r+i0^+}\right)\sum_{v,c}A_r(v,c)\phi_c(\boldsymbol{r}_1)\phi_v^*(\boldsymbol{r}_1') \times\left[\theta(\tau_1)e^{-i\varepsilon_c^{\rm QP}\tau_1}+\theta(-\tau_1)e^{-i\varepsilon_v^{\rm QP}\tau_1}\right]. \tag{A.17}$$

Here, the first negative sign comes from Eq. (A.12a), and the second negative sign inside the parenthesis comes from Eq. (A.11). Eq. (A.17) in the limit $\tau_1=-0^+$ forms the contribution from the left-hand side of the BSE (A.4)

$$\frac{ie^{-i\omega t_1}}{\omega-\Omega_r+i0^+}\sum_{v,c}A_r(v,c)\phi_c(\boldsymbol{r}_1)\phi_v^*(\boldsymbol{r}_1'). \tag{A.18}$$

Lastly, we focus on the second term of the right-hand side of the BSE (A.4). We multiply it by Eq. (A.13) and integrate with respect to $\boldsymbol{r}_2$ and $\boldsymbol{r}_2'$. At $t_1=t_1'$, the time-dependent part of $G(x_1,x_3)G(x_3',x_1')$ can be expressed (by keeping only the contributions where $\boldsymbol{r}_1$ corresponds to the conduction band (c) and $\boldsymbol{r}_1'$ corresponds to the valence band (v)) as follows:

$$\begin{aligned}&G(t_1-t_3)G(t_3'-t_1)\\ &=\sum_c\int\frac{d\omega_1}{2\pi}\frac{e^{-i\omega_1(t_1-t_3)}}{\omega_1-\varepsilon_c^{\rm QP}+i0^+}\sum_v\int\frac{d\omega_2}{2\pi}\frac{e^{-i\omega_2(t_3'-t_1)}}{\omega_2-\varepsilon_v^{\rm QP}-i0^+}\\ &=\sum_{c,v}\int\frac{d\omega_1d\omega_2}{(2\pi)^2}\frac{e^{-i(\omega_1-\omega_2)t_1}e^{i(\omega_1-\omega_2)t^3}e^{i(\omega_1+\omega_2)\tau_3/2}}{(\omega_1-\varepsilon_c^{\rm QP}+i0^+)(\omega_2-\varepsilon_v^{\rm QP}-i0^+)}.\end{aligned} \tag{A.19}$$

The kernel $\Xi(x_3,x_4;x_3',x_4')$ depend on t_3 and t_3' only through $\tau_3=t_3-t_3'$, and, due to the δ-functions of this kernel, the correlation function $L(x_4',x_2;x_4,x_2')$ of the form (A.10) depends on t_3 and t_3' only through $\tau_3=t_3-t_3'$ except for the phase factor $e^{-i\omega t^3}$. Therefore, after multiplying all these factors together, we can perform the integral with respect to the intermediate time $t^3=(t_3+t_3')/2$ (by noting that this integral becomes $2\pi\delta(\omega_1-\omega_2-\omega)$, which leaves only the $\omega_2=\omega_1-\omega$ term in Eq. (A.19), and by performing the ω_1 contour integration separately for $\tau_3>0$ and $\tau_3<0$) as

$$\begin{aligned}&\int_{-\infty}^{\infty}e^{-i\omega t^3}G(x_1,x_3)G(x_3',x_1')dt^3\\ &=ie^{-i\omega t_1}e^{i\omega|\tau_3|/2}\sum_{c,v}\frac{\theta(\tau_3)e^{i\varepsilon_v^{\rm QP}\tau_3}+\theta(-\tau_3)e^{i\varepsilon_c^{\rm QP}\tau_3}}{\omega-(\varepsilon_c^{\rm QP}-\varepsilon_v^{\rm QP})}\phi_c(\boldsymbol{r}_1)\phi_c^*(\boldsymbol{r}_3)\phi_v(\boldsymbol{r}_3')\phi_v^*(\boldsymbol{r}_1').\end{aligned} \tag{A.20}$$

For the exchange term, the kernel $-iv(x_3,x_4)$ acts at the same time $t_3=t_4$ only, and the left arms of the correlation function are closed. To proceed, we multiply $L(x_4',x_2;x_4,x_2')$ by Eq. (A.13). After setting $x_4=x_4'$, we can rewrite it as Eq. (A.17), replacing both $\boldsymbol{r}_1$ and $\boldsymbol{r}_1'$ with $\boldsymbol{r}_4$, while also substituting τ_1 with $\tau_3=-0^+$. Next, we multiply this modified expression by Eq. (A.20) with $\boldsymbol{r}_3=\boldsymbol{r}_3'$. By integrating the resulting expression with respect to $\boldsymbol{r}_3$ and $\boldsymbol{r}_4$, we obtain the exchange term

$$\begin{aligned}&ie^{-i\omega t_1}\sum_{c,v}\frac{\phi_c(\boldsymbol{r}_1)\phi_v^*(\boldsymbol{r}_1')}{\omega-(\varepsilon_c^{\rm QP}-\varepsilon_v^{\rm QP})}(-i)\int\phi_c^*(\boldsymbol{r}_3)\phi_v(\boldsymbol{r}_3)\frac{1}{|\boldsymbol{r}_3-\boldsymbol{r}_4|}\\ &\times(-1)\left(\frac{-i}{\omega-\Omega_r+i0^+}\right)\sum_{v',c'}A_r(v',c')\phi_{c'}(\boldsymbol{r}_4)\phi_{v'}^*(\boldsymbol{r}_4)d\boldsymbol{r}_3d\boldsymbol{r}_4.\end{aligned} \tag{A.21}$$

For the direct term, we start with Eq. (A.17), in which x_1 and x_1' are replaced by x_3 and x_3'. We multiply this expression by Eq. (A.20) and by the dynamically screened Coulomb interaction ($iW(\boldsymbol{r}_3,\boldsymbol{r}_3';\tau_3)=i\int e^{-i\omega'\tau_3}W(\boldsymbol{r}_3,\boldsymbol{r}_3';\omega')\,d\omega'/2\pi$). Next, integrating it with respect to $\boldsymbol{r}_3$, $\boldsymbol{r}_3'$, and τ_3, we obtain the direct term

$$\begin{aligned}&ie^{-i\omega t_1}\sum_{c,v}\frac{\phi_c(\boldsymbol{r}_1)\phi_v^*(\boldsymbol{r}_1')}{\omega-(\varepsilon_c^{\rm QP}-\varepsilon_v^{\rm QP})}\int\phi_c^*(\boldsymbol{r}_3)\phi_v(\boldsymbol{r}_3')\int_{-\infty}^{\infty}d\tau_3\,e^{i\omega|\tau_3|/2}\\ &\times\frac{i}{2\pi}\int d\omega'e^{-i\omega'\tau_3}W(\boldsymbol{r}_3,\boldsymbol{r}_3';\omega')(-1)\left(\frac{-ie^{i\omega|\tau_3|/2}}{\omega-\Omega_r+i0^+}\right)\\ &\times\sum_{v',c'}A_r(v',c')\phi_{c'}(\boldsymbol{r}_3)\phi_{v'}^*(\boldsymbol{r}_3')\\ &\times\left[\theta(\tau_3)e^{i(\varepsilon_v^{\rm QP}-\varepsilon_{c'}^{\rm QP})\tau_3}+\theta(-\tau_3)e^{i(\varepsilon_c^{\rm QP}-\varepsilon_{v'}^{\rm QP})\tau_3}\right]d\boldsymbol{r}_3d\boldsymbol{r}_3'\\ &=ie^{-i\omega t_1}\sum_{c,v}\frac{\phi_c(\boldsymbol{r}_1)\phi_v^*(\boldsymbol{r}_1')}{\omega-(\varepsilon_c^{\rm QP}-\varepsilon_v^{\rm QP})}i\int\frac{\phi_c^*(\boldsymbol{r}_3)\phi_v(\boldsymbol{r}_3')}{\omega-\Omega_r+i0^+}\end{aligned}$$

$$\times \frac{i}{2\pi}\int d\omega' W(\boldsymbol{r}_3,\boldsymbol{r}'_3;\omega')\sum_{v',c'} A_r(v',c')\phi_{c'}(\boldsymbol{r}_3)\phi^*_{v'}(\boldsymbol{r}'_3)d\boldsymbol{r}_3 d\boldsymbol{r}'_3$$
$$\times \left[\int_0^\infty d\tau_3 e^{i(\omega-\omega'+\varepsilon_v^{\rm QP}-\varepsilon_{c'}^{\rm QP}+i0^+)\tau_3}+\int_{-\infty}^0 d\tau_3 e^{i(-\omega-\omega'+\varepsilon_c^{\rm QP}-\varepsilon_{v'}^{\rm QP}-i0^+)\tau_3}\right]$$
$$= ie^{-i\omega t_1}\sum_{c,v}\frac{\phi_c(\boldsymbol{r}_1)\phi^*_v(\boldsymbol{r}'_1)}{\omega-(\varepsilon_c^{\rm QP}-\varepsilon_v^{\rm QP})}\,i\int\frac{\phi^*_c(\boldsymbol{r}_3)\phi_v(\boldsymbol{r}'_3)}{\omega-\Omega_r+i0^+}$$
$$\times \frac{i}{2\pi}\int d\omega' W(\boldsymbol{r}_3,\boldsymbol{r}'_3;\omega')\sum_{v',c'} A_r(v',c')\phi_{c'}(\boldsymbol{r}_3)\phi^*_{v'}(\boldsymbol{r}'_3)d\boldsymbol{r}_3 d\boldsymbol{r}'_3.$$
$$\times\left[\frac{i}{\omega-\omega'-(\varepsilon_{c'}^{\rm QP}-\varepsilon_v^{\rm QP})+i0^+}+\frac{i}{\omega+\omega'-(\varepsilon_c^{\rm QP}-\varepsilon_{v'}^{\rm QP})+i0^+}\right] \quad (A.22)$$

In the last two denominators, ω can be replaced by the resulting PAE, Ω_r.

To derive the matrix eigenvalue equation for the BSE, we combine all these terms on both sides of the BSE (A.4). Multiplying both sides by $\phi^*_c(\boldsymbol{r}_1)\phi_v(\boldsymbol{r}'_1)$, and integrating them with respect to $\boldsymbol{r}_1$ and $\boldsymbol{r}'_1$, we obtain the final equation

$$(\varepsilon_c^{\rm QP}-\varepsilon_v^{\rm QP})A_r(v,c)=\Omega_r A_r(v,c)-\sum_{v',c'}X_{vc;v'c'}A_r(v',c')$$
$$+\sum_{v',c'}W_{cv;c'd'}A_r(v',c'), \quad (A.23)$$

where the exchange term is given by Eq. (12), i.e.,

$$X_{vc;v'c'}=\int\phi^*_c(\boldsymbol{r}_3)\phi_v(\boldsymbol{r}_3)\frac{1}{|\boldsymbol{r}_3-\boldsymbol{r}_4|}\phi_{c'}(\boldsymbol{r}_4)\phi^*_{v'}(\boldsymbol{r}_4)d\boldsymbol{r}_3 d\boldsymbol{r}_4, \quad (A.24)$$

and the direct term is given by Eq. (9) (Note that there is a typo in the pioneering papers [71]), i.e.,

$$W_{vc;v'c'}=i\int\frac{d\omega'}{2\pi}\phi^*_c(\boldsymbol{r}_3)\phi_v(\boldsymbol{r}'_3)W(\boldsymbol{r}_3,\boldsymbol{r}'_3;\omega')\left[\frac{1}{\Omega_r-\omega'-(\varepsilon_{c'}^{\rm QP}-\varepsilon_v^{\rm QP})+i0^+}\right.$$
$$\left.+\frac{1}{\Omega_r+\omega'-(\varepsilon_c^{\rm QP}-\varepsilon_{v'}^{\rm QP})+i0^+}\right]\phi_{c'}(\boldsymbol{r}_3)\phi^*_{v'}(\boldsymbol{r}'_3)d\boldsymbol{r}_3 d\boldsymbol{r}'_3. \quad (A.25)$$

To avoid the ω' integration in Eq. (A.25), we can utilize the GPP model [71] or other plasmon pole models [81,82], as well as static approximations [54]. However, prior to applying these approximations, it is better to separate the bare Coulomb term from Eq. (A.25) as expressed in Eq. (10). This is because the bare Coulomb term must be treated with high precision, especially in all-electron calculations. The dynamically screened Coulomb interaction W is Fourier transformed into the reciprocal space as

$$W(\boldsymbol{r},\boldsymbol{r}';\omega')=\sum_{\boldsymbol{G}\boldsymbol{G}'}e^{i\boldsymbol{G}\cdot\boldsymbol{r}}W_{\boldsymbol{G}\boldsymbol{G}'}(\omega')e^{-i\boldsymbol{G}\cdot\boldsymbol{r}'}. \quad (A.26)$$

Hereafter, we always assume that the momentum transfer is $\boldsymbol{q}=0$. Then, the symbolic relation $W=\varepsilon^{-1}v$ can be written explicitly as

$$W_{\boldsymbol{G}\boldsymbol{G}'}(\omega')=\varepsilon^{-1}_{\boldsymbol{G}\boldsymbol{G}'}(\omega')v(\boldsymbol{G}'), \quad (A.27)$$

where $v(\boldsymbol{G})=4\pi/\Omega|\boldsymbol{G}|^2$ is the Fourier transform of the bare Coulomb interaction with Ω being the volume of the supercell. Under the GPP model at $\boldsymbol{q}=0$, we separate $\varepsilon^{-1}_{\boldsymbol{G}\boldsymbol{G}'}(\omega')$ as [44]

$$\varepsilon^{-1}_{\boldsymbol{G}\boldsymbol{G}'}(\omega')=\delta_{\boldsymbol{G}\boldsymbol{G}'}+\frac{\Omega^2_{\boldsymbol{G}\boldsymbol{G}'}}{2\widetilde{\omega}_{\boldsymbol{G}\boldsymbol{G}'}}\left[\frac{1}{\omega'-\widetilde{\omega}_{\boldsymbol{G}\boldsymbol{G}'}+i0^+}-\frac{1}{\omega'+\widetilde{\omega}_{\boldsymbol{G}\boldsymbol{G}'}-i0^+}\right]. \quad (A.28)$$

Here, the first term $\delta_{\boldsymbol{G}\boldsymbol{G}'}$ is the Fourier transformation of 1, which represents the bare Coulomb term v in $W=\varepsilon^{-1}v=v+(\varepsilon^{-1}-1)v$, while the second term corresponds to $(\varepsilon^{-1}-1)v$. The symbols $\Omega^2_{\boldsymbol{G}\boldsymbol{G}'}$ and $\widetilde{\omega}_{\boldsymbol{G}\boldsymbol{G}'}$ are defined, respectively, as [44]

$$\Omega^2_{\boldsymbol{G}\boldsymbol{G}'}=4\pi\frac{\boldsymbol{G}\cdot\boldsymbol{G}'}{|\boldsymbol{G}|^2}\rho(\boldsymbol{G}-\boldsymbol{G}'), \quad (A.29)$$

$$\widetilde{\omega}^2_{\boldsymbol{G}\boldsymbol{G}'}=\frac{\Omega^2_{\boldsymbol{G}\boldsymbol{G}'}}{\delta_{\boldsymbol{G}\boldsymbol{G}'}-\varepsilon^{-1}_{\boldsymbol{G}\boldsymbol{G}'}(0)}. \quad (A.30)$$

Then, in the ω' integration of Eq. (A.25), the first term becomes the bare Coulomb term $U_{vc;v'c'}$ given by Eq. (11),

$$U_{vc;v'c'}=\int\phi^*_c(\boldsymbol{r})\phi_{c'}(\boldsymbol{r})\frac{1}{|\boldsymbol{r}-\boldsymbol{r}'|}\phi_v(\boldsymbol{r}')\phi^*_{v'}(\boldsymbol{r}')\,d\boldsymbol{r}d\boldsymbol{r}', \quad (A.31)$$

which is expressed in the reciprocal space as

$$U_{vc;v'c'}=\sum_{\boldsymbol{G}}{}'\langle c\,|\,e^{i\boldsymbol{G}\cdot\boldsymbol{r}}\,|\,c'\rangle\langle v'\,|\,e^{-i\boldsymbol{G}\cdot\boldsymbol{r}'}\,|\,v\rangle v(\boldsymbol{G}), \quad (A.32)$$

where $\sum'_{\boldsymbol{G}}$ means that $\boldsymbol{G}=0$ is excluded from the summation in the diagonal terms $c=c'$ and $v=v'$ for the reason discussed around Eq. (13) in Section 4. In the off-diagonal terms $c\neq c'$ or $v\neq v'$, the $\boldsymbol{G}=0$ term automatically vanishes because $\langle c\,|\,c'\rangle=0$ or $\langle v\,|\,v'\rangle=0$. The second term becomes the remaining correlation term $S_{vc;v'c'}$, which is given within the GPP model by [71]

$$S_{vc;v'c'}=\sum_{\boldsymbol{G}}\sum_{\boldsymbol{G}'}\langle c\,|\,e^{i\boldsymbol{G}\cdot\boldsymbol{r}}\,|\,c'\rangle\langle v'\,|\,e^{-i\boldsymbol{G}'\cdot\boldsymbol{r}'}\,|\,v\rangle$$
$$\times\frac{\Omega^2_{\boldsymbol{G}\boldsymbol{G}'}}{2\widetilde{\omega}_{\boldsymbol{G}\boldsymbol{G}'}}\left[\frac{1}{\Omega_r-(\varepsilon_{c'}^{\rm QP}-\varepsilon_v^{\rm QP})-\widetilde{\omega}_{\boldsymbol{G}\boldsymbol{G}'}}\right.$$
$$\left.+\frac{1}{\Omega_r-(\varepsilon_c^{\rm QP}-\varepsilon_{v'}^{\rm QP})-\widetilde{\omega}_{\boldsymbol{G}\boldsymbol{G}'}}\right]v(\boldsymbol{G}'). \quad (A.33)$$

If $1/|\boldsymbol{G}|^2$ and $1/|\boldsymbol{G}'|^2$ in $\Omega^2_{\boldsymbol{G}\boldsymbol{G}'}$ and $v(\boldsymbol{G}')$ are replaced with some nonzero values in the limit $\boldsymbol{G},\boldsymbol{G}'\to 0$ [78], the $\boldsymbol{G}=0$ and/or $\boldsymbol{G}'=0$ contributions to $S_{vc;v'c'}$ automatically vanish due to the form of $\Omega^2_{\boldsymbol{G}\boldsymbol{G}'}$ in Eq. (A.29). The same situation happens also when the GPP model is directly used in $W_{vc;v'c'}$. In the reciprocal space, the exchange term (A.24) is expressed as

$$X_{vc;v'c'}=\sum_{\boldsymbol{G}}\langle c\,|\,e^{i\boldsymbol{G}\cdot\boldsymbol{r}}\,|\,v\rangle\langle v'\,|\,e^{-i\boldsymbol{G}\cdot\boldsymbol{r}'}\,|\,c'\rangle v(\boldsymbol{G}). \quad (A.34)$$

Note that, here again, the $\boldsymbol{G}=0$ term in the summation vanishes because $\langle c\,|\,v\rangle=\langle v'\,|\,c'\rangle=0$.

For the evaluation of $U_{vc;v'c'}$ and $X_{vc;v'c'}$ terms as well as the Fock exchange term in the GW level, we excluded the fully on-site AO-only contributions, which are separately calculated in a single integral along the radial direction, as accurately as possible, using analytic integral forms of the Poisson equation for one-center problem.

Up to now, we have ignored electron spins. However, it is required to consider the spin state of each level, in order to distinguish the singlet and triplet excited (exciton) states. Indeed, the direct $W_{vc;v'c'}$ term exists only when the spin states of v and v' are the same ($\uparrow\uparrow$ or $\downarrow\downarrow$) and the spin states of c and c' are the same, while the exchange $X_{vc;v'c'}$ term exists only when the spin states of v and c are the same and the spin states of v' and c' are the same. Therefore, considering 4×4 matrix consisting of $\uparrow\uparrow$, $\uparrow\downarrow$, $\downarrow\uparrow$, and $\downarrow\downarrow$ rows and columns, the global matrix form of the BSE becomes (note that each matrix element is also the matrix)

$$\begin{bmatrix} D+X & 0 & 0 & X\\ 0 & D & 0 & 0\\ 0 & 0 & D & 0\\ X & 0 & 0 & D+X\end{bmatrix}\begin{bmatrix}A_r^{\uparrow\uparrow}\\A_r^{\uparrow\downarrow}\\A_r^{\downarrow\uparrow}\\A_r^{\downarrow\downarrow}\end{bmatrix}=\Omega_r\begin{bmatrix}A_r^{\uparrow\uparrow}\\A_r^{\uparrow\downarrow}\\A_r^{\downarrow\uparrow}\\A_r^{\downarrow\downarrow}\end{bmatrix}, \quad (A.35)$$

where the matrix elements of D ($D_{vc;v'c'}$) are defined in Eq. (8). This global matrix eigenvalue equation can readily be solved to yield one singlet solution (5) and three degenerate triplet solutions (6). Each solution is, of course, the matrix eigenvalue equation, either the singlet Eq. (5) or the (triply degenerate) triplet Eq. (6). The full 8×8 matrix form including not only $A_r^{\sigma\sigma'}$ but also $B_r^{\sigma\sigma'}$ beyond the Tamm–Dancoff approximation can be found in Ref. [58].

Data availability

Data will be made available on request.

References

[1] A. Fujishima, K. Honda, Electrochemical photolysis of water at a semiconductor electrode, Nature 238 (1972) 37–38, http://dx.doi.org/10.1038/238037a0.

[2] H.P. Maruska, A.K. Ghosh, Photocatalytic decomposition of water at semiconductor electrodes, Sol. Energy 20 (1978) 443–458, http://dx.doi.org/10.1016/0038-092X(78)90061-0.

[3] Hisashi Harada, T. Ueda, Photocatalytic activity of ultra-fine rutile in methanol-water solution and dependence of activity on particle size, Chem. Phys. Lett. 106 (1984) 229–231, http://dx.doi.org/10.1016/0009-2614(84)80231-6.

[4] A. Fujishima, T.N. Rao, D.A. Tryk, Titanium dioxide photocatalysis, J. Photochem. Photobiol. C Photochem. Rev. 1 (2000) 1–21, http://dx.doi.org/10.1016/S1389-5567(00)00002-2.

[5] R.W. Matthews, Solar-electric water purification using photocatalytic oxidation with TiO_2 as a stationary phase, Sol. Energy 38 (1987) 405–413, http://dx.doi.org/10.1016/0038-092X(87)90021-1.

[6] R. Wang, K. Hashimoto, A. Fujishima, M. Chikuni, E. Kojima, A. Kitamura, M. Shimohigoshi, T. Watanabe, Photogeneration of highly amphiphilic TiO_2 surfaces, Adv. Mater. 10 (1998) 135–138, http://dx.doi.org/10.1002/(SICI)1521-4095(199801)10:2<135::AID-ADMA135>3.0.CO;2-M.

[7] C. Longo, A.F. Nogueira, M.-A. De Paoli, H. Cachet, Solid-state and flexible dye-sensitized TiO_2 solar cells: a study by electrochemical impedance spectroscopy, J. Phys. Chem. B 106 (2002) 5925–5930, http://dx.doi.org/10.1021/jp014456u.

[8] K. Sunada, T. Watanabe, K. Hashimoto, Studies on photokilling of bacteria on TiO_2 thin film, J. Photochem. Photobiol. A 156 (2003) 227–233, http://dx.doi.org/10.1016/S1010-6030(02)00434-3.

[9] R. Carbone, I. Marangi, A. Zanardi, L. Giorgetti, E. Chierici, G. Berlanda, A. Podest/'a, F. Fiorentini, G. Bongiorno, P. Piseri, P.G. Pelicci, P. Milani, Biocompatibility of cluster-assembled nanostructured TiO_2 with primary and cancer cells, Biomater. 27 (2006) 3221–3229, http://dx.doi.org/10.1016/j.biomaterials.2006.01.056.

[10] J.M.D. Coey, S.A. Chambers, Oxide dilute magnetic semiconductors—fact or fiction? MRS Bull. 33 (2008) 1053–1058, http://dx.doi.org/10.1557/mrs2008.225.

[11] H. Saadaoui, X. Luo, Z. Salman, X.Y. Cui, N.N. Bao, P. Bao, R.K. Zheng, L.T. Tseng, Y.H. Du, T. Prokscha, A. Suter, T. Liu, Y.R. Wang, S. Li, J. Ding, S.P. Ringer, E. Morenzoni, J.B. Yi, Intrinsic ferromagnetism in the diluted magnetic semiconductor Co:TiO_2, Phys. Rev. Lett. 117 (2016) 227202, http://dx.doi.org/10.1103/PhysRevLett.117.227202.

[12] B. Prajapati, S. Kumar, M. Kumar, S. Chatterjeeb, A.K. Ghosh, Investigation of the physical properties of Fe:TiO_2-diluted magnetic semiconductor nanoparticles, J. Mater. Chem. C 5 (2017) 4257–4267, http://dx.doi.org/10.1039/C7TC00233E.

[13] N. Fajariah, W.A.E. Prabowo, F. Fathurrahman, A. Melati, H.K. Dipojono, The investigation of electronic structure of transition metal doped TiO_2 for diluted magnetic semiconductor applications: A first principle study, Procedia Eng. 170 (2017) 141–147, http://dx.doi.org/10.1016/j.proeng.2017.03.032.

[14] R.C. da Silva, E. Alves, M.M. Cruz, Conductivity behaviour of Cr implanted TiO_2, Nucl. Instrum. Methods Phys. Res. B 191 (2002) 158–162, http://dx.doi.org/10.1016/S0168-583X(02)00541-4.

[15] E. Dy, R. Hui, J. Zhang, Z.-S. Liu, Z. Shi, Electronic conductivity and stability of doped titania ($Ti_{1-x}M_xO_2$, M = Nb, Ru, and Ta) – A density functional theory-based comparison, J. Phys. Chem. C 114 (2010) 13162–13167, http://dx.doi.org/10.1021/jp100826g.

[16] P. Triggs, F. Lévy, Optical and electronic properties of ruthenium-doped TiO_2, Phys. Status Solidi (b) 129 (1985) 363–374, http://dx.doi.org/10.1002/pssb.2221290136.

[17] L. Kernazhitsky, V. Shymanovska, T. Gavrilko, V. Naumov, V. Kshnyakin, T. Khalyavka, A comparative study of optical absorption and photocatalytic properties of nanocrystalline single-phase anatase and rutile TiO_2 doped with transition metal cations, J. Solid State Chem. 198 (2013) 511–519, http://dx.doi.org/10.1016/j.jssc.2012.11.015.

[18] K.A. Rahman, N. Sharma, A.J. Atanacio, T. Bak, E.D. Wachsman, M. Moffitt, J. Nowotny, Chromium segregation in Cr-doped TiO_2 (rutile): impact of oxygen activity, Ionics 25 (2019) 3363–3372, http://dx.doi.org/10.1007/s11581-018-2828-4.

[19] C. Gionco, A. Battiato, E. Vittone, M.C. Paganini, E. Giamello, Structural and spectroscopic properties of high temperature prepared ZrO_2-TiO_2 mixed oxides, J. Solid State Chem. 201 (2013) 222–228, http://dx.doi.org/10.1016/j.jssc.2013.02.040.

[20] M.A.R. Sarker, Optical properties of Al- and Zr-doped rutile single crystals grown by tilting-mirror-type floating zone method and study of structure–property relationships by first principle calculations, J. Inorg. Chem. 2014 (2014) 274165, http://dx.doi.org/10.1155/2014/274165.

[21] F. Ayedun, P.O. Adebambo, B.I. Adetunji, V.C. Ozebo, J.A. Oguntuase, G.A. Adebayo, Increased malleability in tetragonal $Zr_xTi_{1-x}O_2$ ternary alloys: First-principles approach, Z. Nat.forsch. A 72 (2017) 567–572, http://dx.doi.org/10.1515/zna-2017-0036.

[22] A. Iwaszuk, M. Nolan, Electronic structure and reactivity of Ce- and Zr-doped TiO_2: Assessing the reliability of density functional theory approaches, J. Phys. Chem. C 115 (2011) 12995–13007, http://dx.doi.org/10.1021/jp203112p.

[23] H. Maleki-Ghaleh, M.S. Shakeri, Z. Dargahi, M. Kavanlouei, H.K. Garabagh, E. Moradpur-Tari, A. Yourdkhani, A. Fallah, A. Zarrabi, B. Koc, M.H. Siadati, Characterization and optical properties of mechanochemically synthesized molybdenum-doped rutile nanoparticles and their electronic structure studies by density functional theory, Mater. Today Chem. 24 (2022) 100820, http://dx.doi.org/10.1016/j.mtchem.2022.100820.

[24] X. Yu, C. Li, Y. Ling, T.-A. Tang, Q. Wu, J. Kong, First principles calculations of electronic and optical properties of Mo-doped rutile TiO_2, J. Alloys Compd. 507 (2010) 33–37, http://dx.doi.org/10.1016/j.jallcom.2010.07.195.

[25] X. Lu, T. Zhao, X. Gao, J. Ren, X. Yan, P. La, Investigation of Mo-, Pt-, and Rh-doped rutile TiO_2 based on first-principles calculations, AIP Adv. 8 (2018) 075014, http://dx.doi.org/10.1063/1.5038776.

[26] A. Soussi, A. Ait hssi, L. Boulkaddat, M. Boujnah, K. Abouabassi, R. Haounati, A. Asbayou, A. Elfanaoui, R. Markazi, A. Ihlal, K. Bouabid, N. El Biaze, First principle study of electronic, optical and electrical properties of Mo doped TiO_2, Comput. Condens. Matter 29 (2021) e00606, http://dx.doi.org/10.1016/j.cocom.2021.e00606.

[27] L.-j. Bai, G. Kou, Z.-y. Gong, Z.-m. Zhao, Effect of Zn and Ti mole ratio on microstructure and photocatalytic properties of magnetron sputtered TiO_2-ZnO heterogeneous composite film, Trans. Nonferr. Met. Soc. China 23 (2013) 3643–3649, http://dx.doi.org/10.1016/S1003-6326(13)62912-X.

[28] N.A. Erfan, M.S. Mahmoud, H.Y. Kim, N.A.M. Barakat, Synergistic doping with Ag, CdO, and ZnO to overcome electron–hole recombination in TiO_2 photocatalysis for effective water photo splitting reaction, Front. Chem. 11 (2023) 1301172, http://dx.doi.org/10.3389/fchem.2023.1301172.

[29] G.H. Mohammed, A.M. Savore, M.H. Shinen, K.A. Adem, Structural and optical properties of CdO doped TiO_2 thin films prepared by pulsed laser deposition, Eng. Tech. J. 33 (B) (2015) 919–931, http://dx.doi.org/10.30684/etj.33.5B.16.

[30] K. Sahbeni, M. Jlassi, S. Khamlich, M. Kandyla, M. Kompitsas, W. Dimassi, Effect of CdO ratios on the structural and optical properties of CdO-TiO_2 nanocomposite thin films, J. Mater. Sci.: Mater. Electron. 31 (2020) 3387–3396, http://dx.doi.org/10.1007/s10854-020-02887-w.

[31] K. Song, X. Han, G. Shao, Electronic properties of rutile TiO_2 doped with 4d transition metals: First-principles study, J. Alloys Compd. 551 (2013) 118–124, http://dx.doi.org/10.1016/j.jallcom.2012.09.077.

[32] M. Saini, M. Kumar, T. Som, Ab initio study of 3d transition metal-doping effects in rutile-TiO_2: Role of bandgap tunability in conductivity behaviour, Appl. Surf. Sci. 418 (2017) 302–307, http://dx.doi.org/10.1016/j.apsusc.2017.01.262.

[33] K. Sato, H. Akai, T. Minamisono, Ab initio calculations of electric field gradients for transition metal impurities in TiO_2, Z. Nat.forsch. 53a (1998) 396–403, http://dx.doi.org/10.1515/zna-1998-6-720.

[34] L.A. Errico, G. Fabricius, Mario Rentería, Metal impurities in an oxide: Ab initio study of electronic and structural properties of Cd in rutile TiO_2, Phys. Rev. B 67 (2003) 144104, http://dx.doi.org/10.1103/PhysRevB.67.144104.

[35] L. Hedin, New method for calculating the one-particle Green's function with application to the electron-gas problem, Phys. Rev. 139 (1965) A796–A823, http://dx.doi.org/10.1103/PhysRev.139.A796.

[36] G. Strinati, Application of the Green's functions method to the study of the optical properties of semiconductors, Nuovo Cimento 11 (1988) 1–86, http://dx.doi.org/10.1007/BF02725962.

[37] A.J. Layzer, Properties of the one-particle Green s function for nonuniform many-Fermion systems, Phys. Rev. 129 (1963) 897–907, http://dx.doi.org/10.1103/PhysRev.129.897.

[38] F. Hüser, T. Olsen, K.S. Thygesen, Quasiparticle GW calculations for solids, molecules, and two-dimensional materials, Phys. Rev. B 87 (2013) 235132, http://dx.doi.org/10.1103/PhysRevB.87.235132.

[39] T. Nakashima, H. Raebiger, K. Ohno, Normalization of exact quasiparticle wave functions in the Green's function method guaranteed by the Ward identity, Phys. Rev. B 104 (2021) L201116, http://dx.doi.org/10.1103/PhysRevB.104.L201116.

[40] K. Ohno, S. Ono, T. Isobe, A simple derivation of the exact quasiparticle theory and its extension to arbitrary initial excited eigenstates, J. Chem. Phys. 146 (2017) 084108, http://dx.doi.org/10.1063/1.4976553.

[41] K. Ohno, K. Esfarjani, Y. Kawazoe, Computational Materials Science: From Ab Initio to Monte Carlo Methods, second ed., Springer-Verlag, Berlin, ISBN: 9783662565407, 2018.

[42] G. Strinati, H.J. Mattausch, W. Hanke, Dynamical aspects of correlation corrections in a covalent crystal, Phys. Rev. B 25 (1982) 2867–2888, http://dx.doi.org/10.1103/PhysRevB.25.2867.

[43] M.S. Hybertsen, S.G. Louie, First-principles theory of quasiparticles: Calculation of band gaps in semiconductors and insulators, Phys. Rev. Lett. 55 (1985) 1418–1421, http://dx.doi.org/10.1103/PhysRevLett.55.1418.

[44] M.S. Hybertsen, S.G. Louie, Electron correlation in semiconductors and insulators: Band gaps and quasiparticle energies, Phys. Rev. B 34 (1986) 5390–5413, http://dx.doi.org/10.1103/PhysRevB.34.5390.

[45] R.W. Godby, M. Schlüter, L.J. Sham, Accurate exchange–correlation potential for silicon and its discontinuity on addition of an electron, Phys. Rev. Lett. 56 (1986) 2415–2418, http://dx.doi.org/10.1103/PhysRevLett.56.2415.

[46] R.W. Godby, M. Schlüter, L.J. Sham, Self-energy operatorsand exchange–correlation potentials in semiconductors, Phys. Rev. B 37 (1988) 10159–10179, http://dx.doi.org/10.1103/PhysRevB.37.10159.

[47] M. Rohlfing, P. Krüger, J. Pollmann, Quasiparticle band-structure calculations for C, Si, Ge, GaAs, and SiC using Gaussian-orbital basis sets, Phys. Rev. B 48 (1993) 17791–17803, http://dx.doi.org/10.1103/PhysRevB.48.17791.

[48] O. Zakharov, A. Rubio, X. Blase, M.L. Cohen, S.G. Louie, Quasiparticle band structures of six II-VI compounds: ZnS, ZnSe, ZnTe, CdS, CdSe, and CdTe, Phys. Rev. B 50 (1994) 10780–10787, http://dx.doi.org/10.1103/PhysRevB.50.10780.

[49] W. Kohn, L.J. Sham, Self-consistent equations including exchange and correlation effects, Phys. Rev. 140 (1965) A1133–A1138, http://dx.doi.org/10.1103/PhysRev.140.A1133.

[50] P. Hohenberg, W. Kohn, Inhomogeneous electron gas, Phys. Rev. 136 (1964) B864–B871, http://dx.doi.org/10.1103/PhysRev.136.B864.

[51] G. Strinati, Effects of dynamical screening on resonances at inner-shell thresholds in semiconductors, Phys. Rev. B 29 (1984) 5718–5726, http://dx.doi.org/10.1103/PhysRevB.29.5718.

[52] G. Onida, L. Reining, R.W. Godby, R. Del Sole, W. Andreoni, Ab Initio calculations of the quasiparticle and absorption spectra of clusters: The sodium tetramer, Phys. Rev. Lett. 75 (1995) 818–821, http://dx.doi.org/10.1103/PhysRevLett.75.818.

[53] M. Rohlfing, S.G. Louie, Excitonic effects and the optical absorption spectrum of hydrogenated Si clusters, Phys. Rev. Lett. 80 (1998) 3320–3323, http://dx.doi.org/10.1103/PhysRevLett.80.3320.

[54] S. Albrecht, L. Reining, R. Del Sole, G. Onida, Ab initio calculation of excitonic effects in the optical spectra of semiconductors, Phys. Rev. Lett. 80 (1998) 4510–4513, http://dx.doi.org/10.1103/PhysRevLett.80.4510.

[55] M. Rohlfing, S.G. Louie, Electron-hole excitations in semiconductors and insulators, Phys. Rev. Lett. 81 (1998) 2312–2315, http://dx.doi.org/10.1103/PhysRevLett.81.2312.

[56] L.X. Benedict, E.L. Shirley, Ab initio calculation of $\epsilon_2(\omega)$ including the electron–hole interaction: Application to GaN and CaF_2, Phys. Rev. B 59 (1999) 5441–5451, http://dx.doi.org/10.1103/PhysRevB.59.5441.

[57] M. Rohlfing, S.G. Louie, Electron–hole excitations and optical spectra from first principles, Phys. Rev. B 62 (2000) 4927–4944, http://dx.doi.org/10.1103/PhysRevB.62.4927.

[58] K. Ohno, Optical properties of alkali-earth atoms and Na_2 calculated by GW and Bethe–Salpeter equations, Sci. Technol. Adv. Mater. 5 (2004) 603–607, http://dx.doi.org/10.1016/j.stam.2004.02.018.

[59] Y. Noguchi, K. Ohno, All-electron first-principles GW + Bethe–Salpeter calculation for optical absorption spectra of sodium clusters, Phys. Rev. A 81 (2010) 045201, http://dx.doi.org/10.1103/PhysRevA.81.045201.

[60] S. Yamada, Y. Noguchi, K. Ishii, D. Hirose, O. Sugino, K. Ohno, Development of the Bethe–Salpeter method considering second-order corrections for a GW electron–hole interaction kernel, Phys. Rev. B 106 (2022) 045113, http://dx.doi.org/10.1103/PhysRevB.106.045113.

[61] G. Kresse, J. Hafner, Ab initio molecular dynamics for liquid metals, Phys. Rev. B 47 (1993) 558–561, http://dx.doi.org/10.1103/PhysRevB.47.558.

[62] J.P. Perdew, A. Zunger, Self-interaction correction to density-functional approximations for many-electron systems, Phys. Rev. B 23 (1981) 5048–5079, http://dx.doi.org/10.1103/PhysRevB.23.5048.

[63] S. Ishii, K. Ohno, Y. Kawazoe, S.G. Louie, Ab initio GW quasiparticle energies of small sodium clusters by an all-electron mixed-basis approach, Phys. Rev. B 63 (2001) 155104, http://dx.doi.org/10.1103/PhysRevB.63.155104.

[64] S. Ishii, K. Ohno, V. Kumar, Y. Kawazoe, Breakdown of time-reversal symmetry of photoemission and its inverse in small silicon clusters, Phys. Rev. B 68 (2003) 195412, http://dx.doi.org/10.1103/PhysRevB.68.195412.

[65] S. Ishii, S. Iwata, K. Ohno, All-electron GW calculations of silicon, diamond, and silicon carbide, Mater. Trans. 51 (2010) 2150–2156, http://dx.doi.org/10.2320/matertrans.M2010303.

[66] M. Zhang, S. Ono, K. Ohno, All-electron GW calculation of rutile TiO_2 with and without Nb impurities, Phys. Rev. B 92 (2015) 035205, http://dx.doi.org/10.1103/PhysRevB.92.035205.

[67] M. Zhang, S. Ono, N. Nagatsuka, K. Ohno, All-electron mixed basis GW calculations of TiO_2 and ZnO crystals, Phys. Rev. B 93 (2016) 155116, http://dx.doi.org/10.1103/PhysRevB.93.155116.

[68] T. Ishikawa, R. Sahara, K. Ohno, K. Ueda, T. Narushima, Electronic structure analysis of light-element-doped anatase TiO_2 using all-electron GW approach, Comput. Mater. Sci. 220 (2023) 112059, http://dx.doi.org/10.1016/j.commatsci.2023.112059.

[69] S. Ono, Y. Noguchi, R. Sahara, Y. Kawazoe, K. Ohno, TOMBO: All-electron mixed-basis approach to condensed matter physics, Comput. Phys. Comm. 189 (2015) 20–30, http://dx.doi.org/10.1016/j.cpc.2014.11.012.

[70] W. Kang, M.S. Hybertsen, Quasiparticle and optical properties of rutile and anatase TiO_2, Phys. Rev. B 82 (2010) 085203, http://dx.doi.org/10.1103/PhysRevB.82.085203.

[71] There is a typo in the last denominator term both in Eq. (2.18) of Ref. [51] and in Eq. (20) of Ref. [57]: ϵ_d (E_v^{QP}) in their equation should read $\epsilon_{d'}$ ($E_{v'}^{\mathrm{QP}}$). In the corresponding expression using the GPP model, there is also a typo in the last denominator term in Eq. (23) of Ref. [57]: E_v^{QP} in their equation should read $E_{v'}^{\mathrm{QP}}$.

[72] L. Chiodo, J.M. Garcia-Lastra, A. Iacomino, S. Ossicini, J. Zhao, H. Petek, A. Rubio, Self-energy and excitonic effects in the electronic and optical properties of TiO_2 crystalline phases, Phys. Rev. B 82 (2010) 045207, http://dx.doi.org/10.1103/PhysRevB.82.045207.

[73] Y. Tezuka, S. Shin, T. Ishii, T. Ejima, S. Suzuki, S. Sato, Photoemission and bremsstrahlung isochromat spectroscopy studies of TiO_2 (Rutile) and $SrTiO_3$, J. Phys. Soc. Japan 63 (1994) 347–357, http://dx.doi.org/10.1143/JPSJ.63.347.

[74] K. Vos, H.J. Krusemeyer, Low temperature electroreflectance of TiO_2, Solid State Commun. 15 (1974) 949–952, http://dx.doi.org/10.1016/0038-1098(74)90701-7.

[75] M. Landmann, E. Rauls, W.G. Schmidt, The electronic structure and optical response of rutile, anatase and brookite TiO_2, J. Phys.: Condens. Matter. 24 (2012) 195503, http://dx.doi.org/10.1088/0953-8984/24/19/195503.

[76] A. Thatribud, Electronic and optical properties of TiO_2 by first-principle calculation (DFT-GW and BSE), Mater. Res. Express 6 (2019) 095021, http://dx.doi.org/10.1088/2053-1591/ab2cad.

[77] M. Cardona, G. Harbeke, Optical properties and band structure of wurtzite-type crystals and rutile, Phys. Rev. 137 (1965) A1467–A1476, http://dx.doi.org/10.1103/PhysRev.137.A1467.

[78] See, for example, Appendix B of Ref. [44]. Also, there are discussions after Eq. (2) of Ref. [79] and after Eq. (9) of [80].

[79] S. Albrecht, G. Onida, L. Reining, Ab initio calculation of the quasiparticle spectrum and excitonic effects in Li_2O, Phys. Rev. B 55 (1997) 10278–10281, http://dx.doi.org/10.1103/PhysRevB.55.10278.

[80] T. Rangel, M.D. Ben, D. Varsano, G. Antonius, F. Bruneval, F.H. da Jornada, M.J. van Setten, O.K. Orhan, D. O'Regan, A. Canning, A. Ferretti, A. Marini, G.-M. Rignanese, J. Deslippe, S.G. Louie, J.B. Neaton, Reproducibility in G_0W_0 calculations for solids, Comput. Phys. Comm. 255 (2020) 107242, http://dx.doi.org/10.1016/j.cpc.2020.107242.

[81] G.E. Engel, B. Farid, Generalized plasmon-pole model and plasmon band structures of crystals, Phys. Rev. B 47 (1993) 15931–15934, http://dx.doi.org/10.1103/PhysRevB.47.15931.

[82] W. von der Linden, P. Horsch, Precise quasiparticle energies and Hartree–Fock bands of semiconductors and insulators, Phys. Rev. B 37 (1988) 8351–8362, http://dx.doi.org/10.1103/PhysRevB.37.8351.

[83] L.J. Sham, T.M. Rice, Many-particle derivation of the effective-mass equation for the Wannier exciton, Phys. Rev. 144 (1966) 708–714, http://dx.doi.org/10.1103/PhysRev.144.708.

[84] Z. Zarhri, A. Benyoussef, A. El Kenz, Theoretical study of TiO_2 doped with single and double impurities, J. Supercond. Nov. Magn. 27 (2014) 1323–1328, http://dx.doi.org/10.1007/s10948-013-2439-2.

[85] G.C. Vásquez, D. Maestre, A. Cremades, J. Ramírez-Castellanos, E. Magnano, S. Nappini, S.Zh. Karazhanov, Understanding the effects of Cr doping in rutile TiO_2 by DFT calculations and X-ray spectroscopy, Sci. Rep. 8 (2018) 8740, http://dx.doi.org/10.1038/s41598-018-26728-3.

[86] G.Y. Csanak, H.S. Taylor, R. Yaris, Green's function technique in atomic and molecular physics, Adv. At. Mol. Phys. 7 (1971) 287–361, http://dx.doi.org/10.1016/S0065-2199(08)60363-2.